Short-Range to Long-Range Ni/Mn Order in LiMn 2– x Ni x O 4 (0.38 ≤ x ≤ 0.50) Positive Electrode Materials: A Gradual Temperature-Driven Sublattice Disorder through Antiphase Boundary Defects

Nicolas Emery, Ankush Bhatia, Yanis Ghaleb, Alexander Mitrushchenkov, Céline Léonard, Jean-Pierre Pereira-Ramos, Rita Baddour-Hadjean, Ronald Smith

Short-range to long-range Ni/Mn order in $LiMn_{2-x}Ni_xO_4$ ($0.38 \leq x \leq 0.50$) positive electrode material: a gradual temperature-driven sublattice disorder through antiphase boundary defects

Nicolas Emery[1,*], Ankush Bhatia[1], Yanis Ghaleb[2], Alexander O. Mitrushchenkov[2], Céline Léonard[2], Jean-Pierre Pereira-Ramos[1], Rita Baddour-Hadjean[1], Ronald I. Smith[3]

[1]Univ Paris-Est Créteil, CNRS, ICMPE (UMR 7182), 2 rue Henri Dunant, F-94320 Thiais, France

[2]MSME, Univ Gustave Eiffel, CNRS, Univ Paris Est Créteil, UMR 8208, F-77454, Marne-la-Vallée, France

[3]ISIS Facility, Rutherford Appleton Laboratory, Didcot, Oxfordshire OX11 0OX, UK

*Corresponding author: emery@icmpe.cnrs.fr

abstract

$LiMn_{2-x}Ni_xO_4$ spinel phases, with their almost flat electrochemical curves composed of two plateaus around 4.7 V *vs* Li^+/Li separated by a voltage difference ΔV of 20 to 60 mV, are good candidates for high power applications. The Ni/Mn order is one of the key parameters in understanding the electrochemical curve shape. In this work, the Ni/Mn order in the nickel-rich region of the spinel $LiMn_{2-x}Ni_xO_4$ solid-solution ($0.38 \leq x \leq 0.50$) has been investigated using *Time-of-Flight Powder Neutron Diffraction* (TOF-PND) and *Density Functional Theory* calculations (DFT). For $LiMn_{2-x}Ni_xO_4$ solid-solution samples prepared between 700 and 900°C, Ni/Mn ordering was found to be retained to room temperature by systematic broadening of diffraction peaks with *hkl* indexes of mixed even/odd parity. This broadening is due to the increasing density of a planar defect called *antiphase domain boundaries* (APB). DFT calculations performed on several Ni/Mn defective configurations and TOF-PND Rietveld refinement indicate that the {100} orientation of the APB boundary is the most probable. Hence, in the whole composition range, a single ordered spinel phase within the space group $P4_332$ with a single *hkl* dependent parameter to represent the APB crossing probability, gives a measure of the Ni/Mn order coherence length. We show that this defect density is driven by the synthesis temperature and the nickel content of the spinel phase. A correlation between the synthesis conditions effect on the local ordering and the voltage profile is given for two Ni/Mn initial ratio (0.4/1.6 and 0.5/1.5). The influence of the synthesis temperature on these two compositions is drastically different: for $LiMn_{1.6}Ni_{0.4}O_4$, with similar APB domain size whatever the temperature, only a slight variation of ΔV is observed. Reversely, for $LiMn_{1.5}Ni_{0.5}O_4$, a strong increase of the of ΔV with the synthesis temperature is evidenced, concomitant with a decrease of the APB domain size and the Ni content.

Introduction

Nickel-substituted lithium manganese oxide spinels $LiMn_{2-x}Ni_xO_4$ ($0.4 \leq x \leq 0.5$) have attracted tremendous attention during the past two decades due to their high working potential along with an interesting theoretical specific capacity of 147 mA h g^{-1} [1,2]. The partial substitution of manganese by nickel ions has several advantages over the unsubstituted $LiMn_2O_4$ phase. First, thanks to the electroactivity of Ni^{2+}/Ni^{3+} and Ni^{3+}/Ni^{4+} redox couples, a significant increase of the overall operating voltage is achieved, up to ~4.7 V vs Li^+/Li, instead of the ~4-4.1 V vs Li^+/Li for $LiMn_2O_4$. Second, the substitution of 0.5 manganese by Ni^{2+} drastically reduces the content of Mn^{3+} ions, which are known to be detrimental for the cycling life due to their solubility in the electrolyte[3]. Moreover, such

composition without critical element [4] and its related structure with a connected 3D diffusion network promoting fast Li^+ diffusion, make it attractive for use in power applications such as zero-emission mobility solutions [5].

The cubic spinel structure can be depicted as a 2x2x2 array of 8 faces centered cubic cells composed of O^{2-} ions, in which one eighth of tetrahedral sites are occupied by Li ions (Figure 1a) and half of the octahedral sites are filled by the transition metals (Ni/Mn) (Figure 1b). The transition metal filled octahedra are linked to one another by an edge, forming arrays along <110> directions (Figure 1c and d).

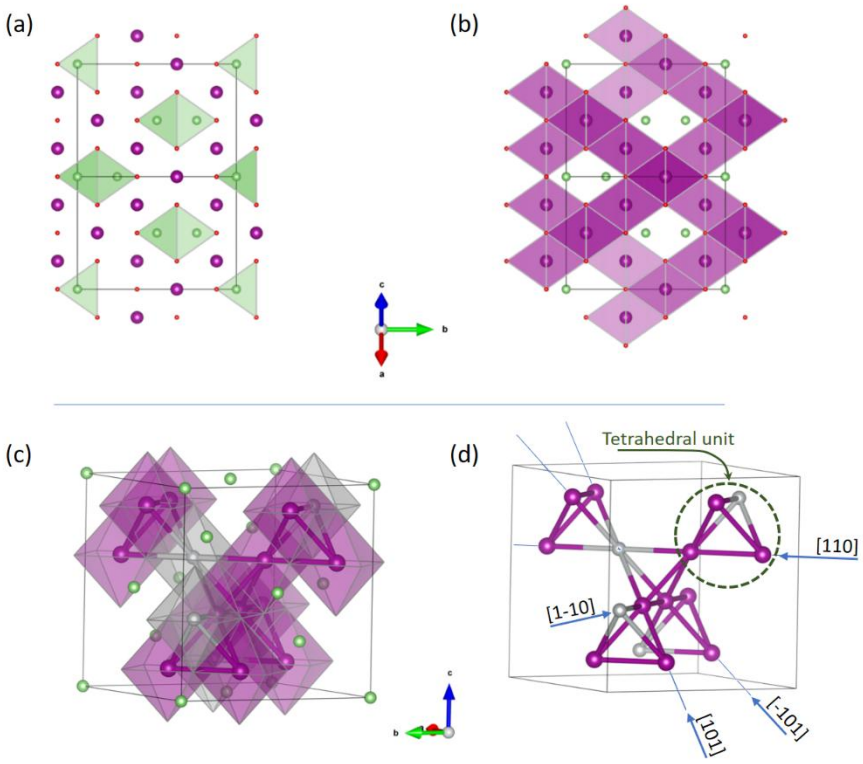

Figure 1: (a) and (b) Projection in the [101] direction of the $LiMn_2O_4$ spinel structure. (a) LiO_4 tetrahedra and (b) MnO_6 octahedra are drawn. (c) 3D representation of ordered $LiMn_{1.5}Ni_{0.5}O_4$ and (d) Ni^{2+} and Mn^{4+} ions distribution in the ordered $LiMn_{1.5}Ni_{0.5}O_4$ structure. Several <110> directions of the Ni/Mn octahedron arrays are displayed. A tetrahedral unit formed by the center of the octahedra in indicated. (red, purple, grey and green spheres are oxygen, manganese, nickel, and lithium ions respectively)

Two long-range structures are usually encountered for $LiMn_{1.5}Ni_{0.5}O_4$: the so-called "disordered" spinel, within the *Fd-3m* space group, and the "ordered" spinel, within the $P4_332$ space group (or its enantiomorphic description with $P4_132$ space group). The "ordered" structure is obtained from thermal treatment around 700°C while the "disordered" one results from a synthesis at higher temperature, usually around 900°C [6]. Then, in the "disordered" description, only 3 distinct Wyckoff positions are needed to fully describe the structure: Ni^{2+} and Mn^{4+} ions are randomly distributed in the *16d* position of the *Fd-3m* space group, lithium fills the *8a* site and oxygen occupies a *32e* site. The Ni^{2+} and Mn^{4+} ions ordering induces a symmetry reduction to the primitive space group $P4_332$. Ideally, in this "ordered" polymorph description, Mn^{4+} ions occupy the *12d* position while the Ni^{2+} ions are in *4a* site. Lithium fills an *8c* site and oxygen ions are distributed over a *24e* and an *8c* Wyckoff positions. In the latter description, arrays of edge-sharing octahedra running along <110> directions possess a particular ordering between Ni^{2+} and Mn^{4+} ions related to the stoichiometry: two successive Ni^{2+} filled octahedra are separated by 3 Mn^{4+} filled octahedra (Figure 1

c and d). Hence, two Ni^{2+} octahedra cannot be linked by an edge within this description. Moreover, centers of $(Mn/Ni)O_6$ octahedra form tetrahedral units connected by the summit to the neighboring units (Figure 1d).

These structural differences are responsible for a subtle variation in their electrochemical profile: the "ordered" phase exhibits an almost flat single plateau at 4.7 V *vs*. Li^+/Li [7]. Open Circuit Voltage measurements of Ariyoshi *et al* [8] evidenced two distinct plateaus, with a small voltage difference ΔE between them, limited to ~20 mV (4.718 and 4.739 V *vs.* Li^+/Li). Differently, the "disordered" phase exhibits two well defined plateaus, separated by a voltage difference ΔV of 40-60 mV [9,10,11,12], and usually a small additional contribution around 4 V is present, indicating the presence of Mn^{3+} ions in the structure.

The above descriptions are idealized views of the $LiMn_{1.5}Ni_{0.5}O_4$ composition. In practice, the preparation conditions affect cationic "order"/"disorder" degree of this particular spinel oxide, which falls in between the "ordered" and "disordered" descriptions, with in addition, deviation from the stoichiometric ratio Ni/Mn = 1/3 [2]. It has been demonstrated that that at higher synthesis temperatures the nickel solubility in the spinel phase is lowered [13,14]. Hence, a secondary Ni-rich rock-salt type phase appears at synthesis temperature over 800°C, and its fraction increases with the temperature. Consequently, the Mn^{3+} contribution observed in galvanostatic curves arises from the temperature-induced nickel sub-stoichiometry [13,14] and/or possible oxygen deficiency [15].

Partial order/disorder in $LiMn_{1.5}Ni_{0.5}O_4$ prepared at different temperatures has been evidenced mainly using neutron scattering techniques [13,16,17,18,19,20] which are particularly suitable due to significantly different manganese and nickel scattering lengths [21]. Based on powder neutron diffraction experiments (PND) [13], Cabana *et al* reported modulation in the background for most of the samples indexed within the "disordered" *Fd-3m* space group. Later, Casas-Cabanas *et al* [17] evidenced a selective broadening of peaks only related to Ni/Mn ordering for samples indexed within the $P4_332$ space group, attributed to the presence of AntiPhase Boundary (APB) defects. These stacking faults are usually observed in various systems such as metallic compounds [22,23] or oxides [24,25,26,27,28]. APB defect has been extensively studied in the cubic intermetallic Cu_3Au [22,29,30]: his defect arises from the nucleation at different nonequivalent sites of ordered phase grains during the transition from a disordered (*Fm3m*) structure to the ordered (*Pm3m*) one [22]. Hence, when those grains come into contact, a phase difference is observed between structure factors of both grains and the additional Cu/Au order induces *hkl* peaks (*hkl* indexes of mixed even/odd parity [29,30]). As a result, a broadening of these reflections is observed, indicating a smaller coherence length compared to the fundamental peaks (*hkl* of same parity), which are common to both structures (*Fm3m* and *Pm3m*). Similar peak broadening was also evidenced on PND patterns for various $LiMn_{1.5}Ni_{0.5}O_4$ samples [18,20] or doped spinel oxides [31,32], figuring a smaller coherent length of the Ni/Mn ordering than the overall spinel framework. Based on Neutron Pair Distribution Function analyses [19,20], apparent "disordered" $LiMn_{1.5}Ni_{0.5}O_4$ exhibits nevertheless similar local structure than the "ordered" polymorph over a limited range. Indeed, the first discrepancies were evidenced at the third nearest Ni/Mn neighbor [19].

The aim of this work is to provide a clear description of the Ni/Mn ordering within the spinel framework in the nickel-rich part of the $LiMn_{2-x}Ni_xO_4$ solid-solution ($0.38 \leq x \leq 0.5$). Based on Time-Of-Flight Neutron Diffraction experiments (TOF-PND), an evaluation of the APB domain size as a function of the synthesis temperature and the nickel content is provided. In addition, the APB influence on the local ordering and the system free energy of $LiMn_{1.5}Ni_{0.5}O_4$ is investigated by DFT calculation. This theoretical approach confirms the low impact of this defect on the local ordering, which is fully consistent with our present experiments and literature data [19,20]. Moreover, a correlation between the Mn^{3+} contribution to the galvanostatic curves can be drown with the Ni/Mn initial ratio and the

Ni-rich rock-salt impurity appearance. Hence, in our synthesis conditions, oxygen vacancies in the spinel framework might be low and most of the oxygen departure recorded in thermogravimetric analysis [14], might be attributed to rock-salt impurity formation.

Experimental and Computational Details

Synthesis and structural characterization

$LiMn_{2-x}Ni_xO_4$ powders with x = 0.38, 0.40, 0.42, 0.44, 0.48 or 0.50, were synthesized through a co-precipitation route using acetates precursors and oxalic acid [33]. Stoichiometric amount of manganese, nickel, and lithium acetates (99% Sigma-Aldrich) were mixed with oxalic acid (1:1 molar ratio of oxalic acid to metal ions) and dissolved in distilled water. The solution was stirred until a green precipitate formed. Products were dried overnight at 110°C and then fired in air for 5h at 490°C to remove organic species. Samples were ground thoroughly then die pressed into pellets (13 mm diameter, thickness ~10 mm). A 48h thermal treatment at a temperature of 700, 800, 850 or 900°C, was performed in air twice on each sample with an intermediate grinding.

Powder X-ray diffraction (XRD) patterns were collected with a Panalytical XPert Pro diffractometer equipped with a Co X-ray tube (λK_α = 1.789 Å) and a linear Pixcell 1D detector. Time-of-flight powder neutron diffraction (TOF-PND) data were collected at ambient temperature at the ISIS neutron spallation source, STFC Rutherford Appleton Laboratory, UK, on GEM diffractometer (x= 0.4, 0.5 prepared at 700°C and 900°C and x=0.44 prepared at 700°C) [34,35,36,37,38,39] or Polaris diffractometer for all the other samples [40, 41].

XRD patterns have been analyzed using Rietveld refinement method with the GSAS ExpGUI package [42,43]. TOF-PND patterns were fitted with BRUKER-AXS TOPAS v4.2 [44] in *launch* mode using macros adapted from Topas Wiki [45,46] and R. E. Dinnebier *et al* [47]. "Goodness of fit" (GOF) and "R-weighted pattern" (Rwp) are defined as [47]:

$$GOF = \sqrt{\frac{\sum w_m \left(Y_{o,m} - Y_{c,m}\right)^2}{M - P}}$$

$$R_{wp} = \sqrt{\frac{\sum w_m \left(Y_{o,m} - Y_{c,m}\right)^2}{\sum w_m {Y_{o,m}}^2}}$$

Where $Y_{o,m}$ and $Y_{c,m}$ are the observed and calculated intensities at point m, $w_m = 1/s(Y_{o,m})^2$ with $s(Y_{o,m})$ being the error in $Y_{o,m}$, M is the number of data points and P, the number of parameters.

The powders were characterized by scanning electron microscopy (SEM), Zeiss, Merlin-type microscope.

Electrochemical characterization

Electrochemical tests were performed in two-electrode configuration using CR2032 coin cells. The positive electrode was composed of 80 wt % of active material, 15 wt % of acetylene black for electrical conductivity, and 5 wt % of PTFE as binder. About 6 mg of this mix was pressed (4 tons/cm²) and placed on a stainless-steel current collector. Li metal was used as negative and reference electrodes and Whatman glass fibers paper separators were soaked with 1 M $LiPF_6$ electrolyte solution (EC:DMC 1:1 in volume). Coin-cells were assembled in argon-filled glovebox with water and

oxygen concentrations lower than 1 ppm. Electrochemical experiments were carried out at 20°C with a VMP3 Biologic potentiostat at a C/10 rate (i.e. 1 $Li^+/LiMn_{2-x}Ni_xO_4$ exchange in 10h).

Density Functional Theory calculations (DFT)

Density Functional Theory calculations were performed with *Vienna Ab initio Simulation Package* [48] using the projector augmented-wave method [49] to describe ion-electron interactions and the exchange-correlation functional by the generalized gradient approximation (GGA) within the Perdew-Burke-Ernzerhof (PBE) framework [50,51]. A Hubbard correction term +U was applied to correctly evaluate the associated redox potential [52,53]. U values were set to 3.9 and 6.2 for Mn and Ni respectively. Several cells and supercells were generated to depict various Ni/Mn disorder and APB defects. The *k*-point sampling has been adjusted for each cell and the high energy cutoff was fixed to 520 eV. All calculations were performed within the *P1* space group to ensure free movement of all species during geometry optimizations. The default thresholds were used: electronic energies were converged to 10^{-4} eV using Gaussian smearing with width of 0.05 eV, and geometry optimization was stopped for energy difference below 10^{-3} eV. We have checked that the tetrahedron method including Blöchl correction gives exactly the same electronic energy as Gaussian smearing.

Results and discussion

Overall analysis of TOF neutron data

It is commonly reported that increasing the $LiMn_{1.5}Ni_{0.5}O_4$ synthesis temperature lowers the degree of Ni/Mn ordering [2,6,13] and increases the average grain size [54]. In the nickel-rich part of the $LiMn_{2-x}Ni_xO_4$ solid-solution ($0.38 \leq x \leq 0.5$), our TOF-PND patterns confirm this trend, as shown for $LiMn_{1.52}Ni_{0.48}O_4$ composition (Figure 2). As a primary observation of Figure 2a, $LiMn_{1.52}Ni_{0.48}O_4$ patterns of samples prepared at temperature of 800°C and higher are easily indexed using the normal spinel structure description within the *Fd-3m* space group, suggesting a random distribution of the Ni^{2+} and Mn^{4+} cations in octahedral sites while the 700°C sample exhibits many extra peaks belonging to the lower symmetry space group, $P4_332$, demonstrating the Ni/Mn ions order (blue marks below 700°C pattern on Figure 2a). Moreover, In accordance with a favored grain growth above 750°C [54], a significant decrease of the peak width is observed for sample prepared at 800°C and higher (Figure 2b). it is confirmed by SEM images recorded from samples prepared at 700°C and 900°C powders (Figure 2d). A careful examination of the background around 1.75 and 2.25 Å in Figure 2a indicates the presence of weak diffuse scattering caused by a remaining Ni^{2+}/Mn^{4+} local ordering and which shows up more clearly in the patterns collected using the low angle detector (Figure 2c). A clear broadening of *110*, *210* and *211* reflections is apparent for 800 and 850°C while a large diffuse peak, composed of the *210* and *211* reflections overlap is still existing on the 900°C pattern, thus indicating the signature of a remaining short-range order between Ni^{2+} and Mn^{4+} ions.

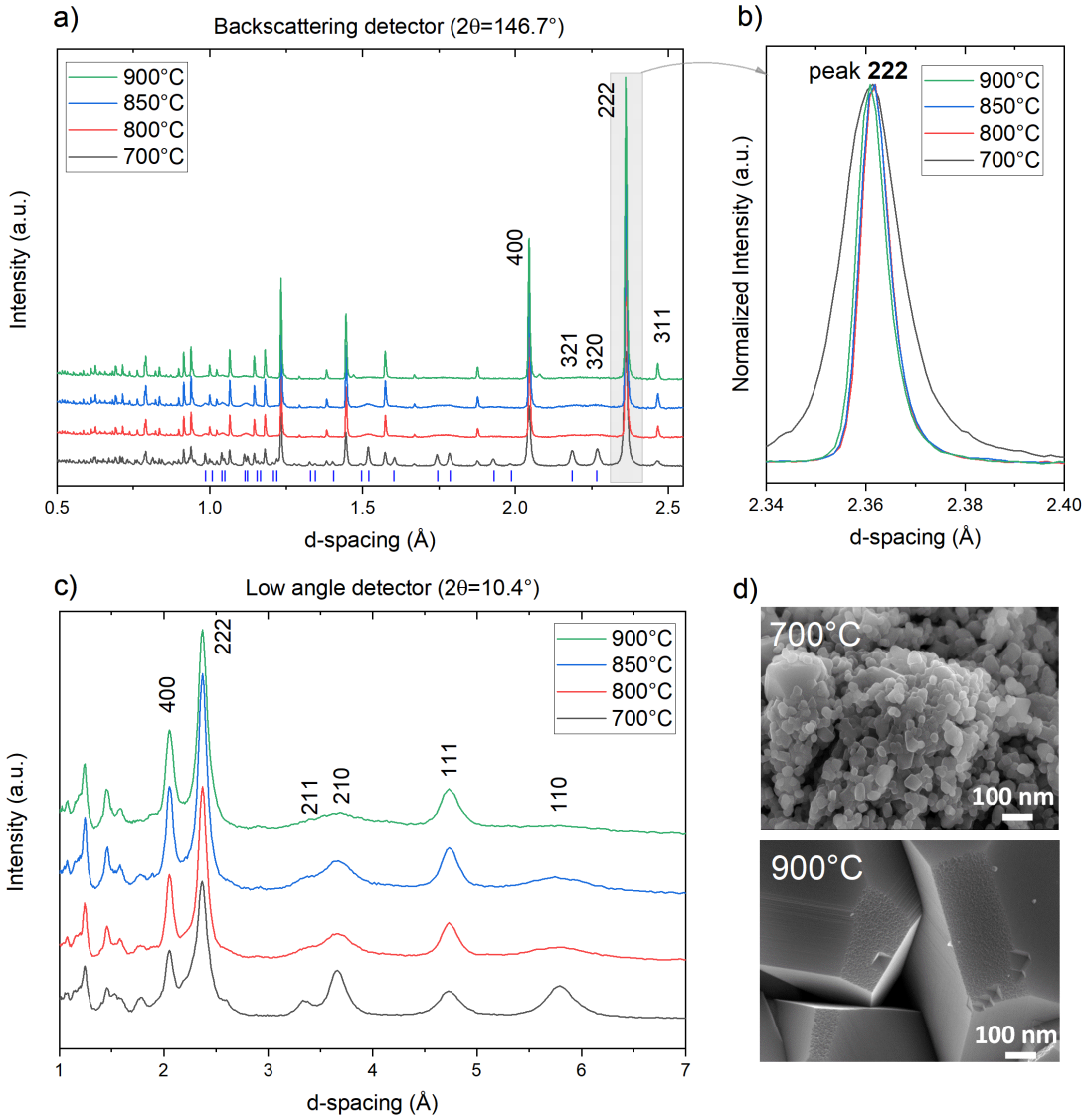

Figure 2: (a) TOF-PND diffraction patterns of $LiMn_{1.52}Ni_{0.48}O_4$ recorded on the Polaris backscattering detector; (b) enlarged view of the 222 peaks; (c) TOF-PND patterns recorded on the low angle detector and (d) SEM images of 700 and 900°C powder. (a) and (c) demonstrate the broadening of the Ni/Mn ordering related peaks (h, k and l of mixed even/odd parity) while (b) and (d) evidence the grain size difference.

Figure 3a and b gather diffraction patterns of $LiMn_{1.62}Ni_{0.38}O_4$ synthesized at different temperatures (0.38 is the lower nickel content sample studied in this work). Whatever the synthesis temperature, a local ordering is evidenced on the low angle detector with the presence of broad *110*, *210* and *211* reflections. Patterns recorded with the backscattering detector only evidence small and broad peaks related to Ni/Mn order. $LiMn_{1.58}Ni_{0.42}O_4$ patterns recorded with the low angle and backscattering detectors are plotted in Figure 3c and 3d respectively. For this composition, the sample prepared at 700°C is easily indexed using the $P4_332$ space group, which demonstrates a clear ordering between Ni and Mn ions. Raising the synthesis temperature leads to a slight peak broadening of *hkl* reflections with mixed odd and even indexes, in line with the reduction of the Ni/Mn ordering size domains. However, compared to $LiMn_{1.52}Ni_{0.48}O_4$ patterns (Figure 2a and c), for synthesis at 800°C and higher, the Ni/Mn ordering still occurs on a longer scale.

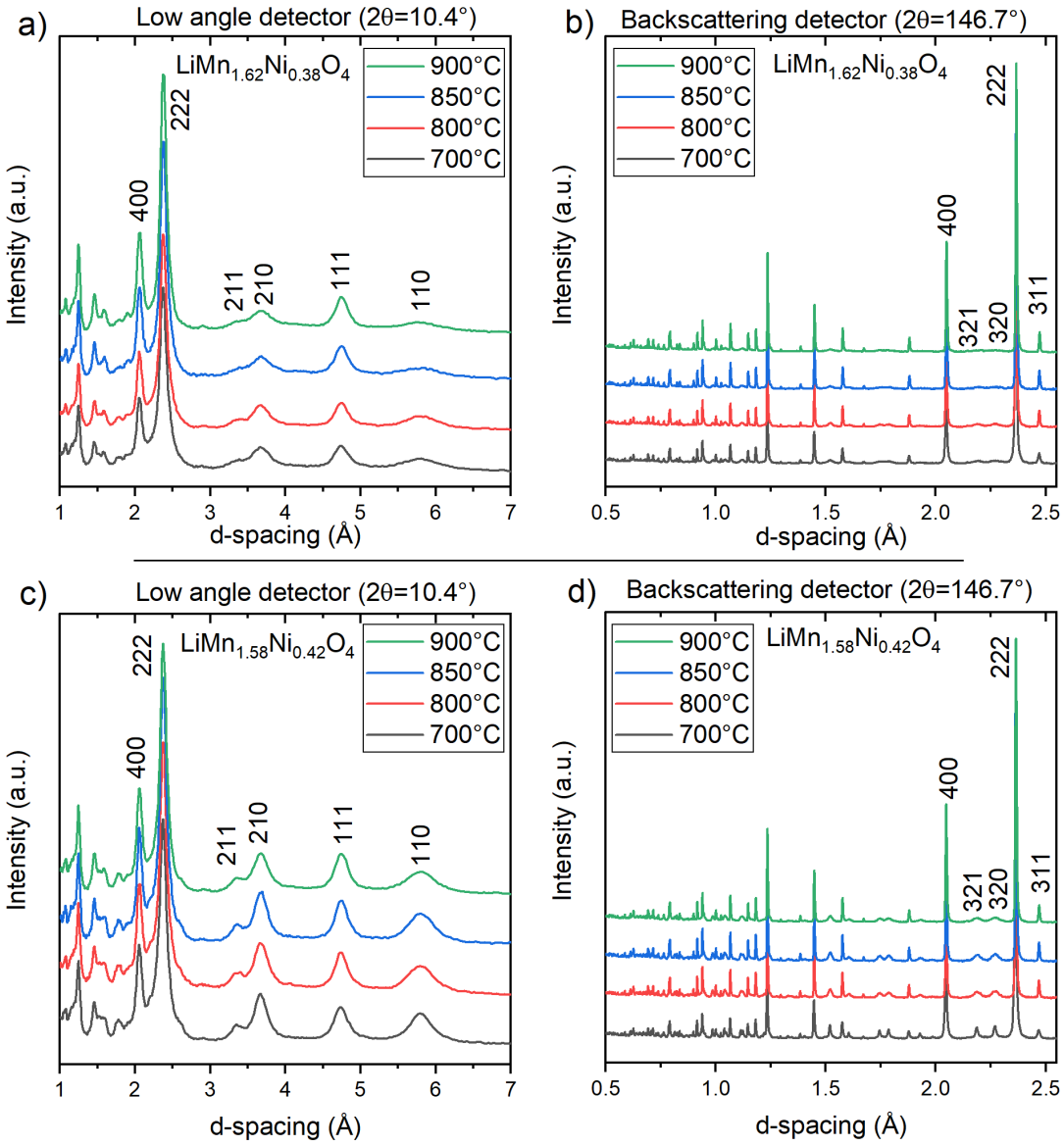

Figure 3: (a) $LiMn_{1.62}Ni_{0.38}O_4$ low angle and (b) backscattering detector diffraction patterns. (c) $LiMn_{1.58}Ni_{0.42}O_4$ low angle and (b) backscattering detector diffraction patterns.

APB-related peak broadening models

To go further in the analysis and evaluate the average coherence lengths of these APB domains, specific peak broadening rules were introduced to the Rietveld refinement procedure. As previously described for TOF diffraction experiment, the sample crystallite size contribution to the peak full width half maximum (FWHM) is given by the expression [47]:

$$fwhm_{hkl}^{TOF} = t_1 (d_{hkl})^2 \frac{1}{D_0} \qquad (1)$$

where $fwhm_{hkl}^{TOF}$ is the full width half maximum of a given *hkl* peak, d_{hkl} is the interplanar distance related to the *hkl* plane, D_0, the average crystallite size, and t_1, one coefficient of the expression linking the neutron *time-of-flight* TOF to the d spacing value ($TOF = t_0 + t_1 d + t_2 d^2$). For reflections with *hkl* indexes of mixed parity, an additional parameter must be introduced to figure out the probability of crossing an APB into a crystallite:

$$fwhm_{hkl}^{TOF} = t_1(d_{hkl})^2 \frac{\delta_{hkl}^{APB}}{D_0} \quad (2)$$

were δ_{hkl}^{APB} is the probability to cross an APB within the crystallite coherence length along the [*hkl*] direction. According to Scardi [23], no general formula exists to account for the APB related peak broadening, since the expression of δ_{hkl}^{apb} is dependent of the lattice orientation of the APB and to the local arrangement at this boundary. Explicit formulae for only few systems such as $AuCu_3$ [22,29,30], were determined for various types of APB. Based on Wilson and Zoldos method devoted to $AuCu_3$ [29], Cheary and Grimes adapted the *hkl* dependence of the APB related peak broadening to the reverse spinel $LiFe_5O_8$ case (with the site distribution $[Fe]_{tetrahedron}[Li_{0.5}Fe_{1.5}]_{octahedron}O_4$ [26]). Peculiarly, additional grain boundary configurations were settled and included in the model to account for the non-centrosymmetric nature of the reverse spinel structure. Hence, 8 different domains are possible, 4 with the *P4₃32* space group defined relative to one another by *a*/2<110> translations and the 4 equivalent enantiomorphs within the *P4₁32* space group. A representation of the 8 possible domains as proposed by Lefebvre *et al* with the associated translation is given in S.I.1 [27]. As indicated in the introduction, ions filling the octahedral sites of the spinel structure form tetrahedra linked to others by their apices (Figure 1d). For the ordered $LiFe_5O_8$ (*P4₃32* space group), the same scheme is present with only one lithium per tetrahedral unit. Therefore, APB domains can be either conservative (i.e. preserved local ordering of the tetrahedral unit) or no-conservative (i.e. the 1:3 ratio of the tetrahedral unit can be broken at the boundary). Only conservative boundary cases were treated in [26] to respect the tetrahedral unit charge invariance principle proposed by Anderson [55]. Based on DFT calculation, Lee and Persson demonstrated for $LiMn_{1.5}Ni_{0.5}O_4$ that nickel filled octahedron are surrounded only by manganese filled octahedra [56], which corresponds to the tetrahedral unit charge invariance principle encountered in $LiFe_5O_8$ [55]. Then, the application of Cheary and Grimes's work to $LiMn_{1.5}Ni_{0.5}O_4$ APB's problem is straightforward since this spinel is isostructural to $LiFe_5O_8$ (Fe^{3+} in *12d* and *8c* positions in $LiFe_5O_8$ are replaced by Mn^{4+} and Li^+ respectively while Li^+ in *4a* site in $LiFe_5O_8$ is replaced by Ni^{2+}). We then used the *hkl* dependent broadening probability to cross an APB within the crystallite size as proposed in [26] to analyze our data. For conservative boundaries forming on {100} planes between two different domains with *h*, *k* and *l* all positive and $h \geq k \geq l$ [26]:

$$\delta_{hkl}^{APB} = \frac{(h+k+l)\delta}{7\sqrt{N}} \quad (3)$$

where $N = h^2 + k^2 + l^2$ and δ the probability to cross an APB. For conservative boundaries forming on {110} planes with *h*, *k* and *l* all positive and with $h \geq k \geq l$ [26]:

$$\delta_{hkl}^{APB} = \frac{(4h + 2k)\delta}{7\sqrt{2N}} \quad (4)$$

In both cases, the mean domain thickness is given by $\frac{7D_0}{\delta_{hkl}^{APB}}$ since for a given orientation domain, 7 possible domains can be encountered (3 with origin translated by a/2<110> and 4 with the enantiomorphic structures). Examples of {100} and {110} planar defect position in the Ni/Mn network are given in S.I.2. Moreover, a random model has been evaluated, where the mean domain thickness is given by $\frac{D_0}{\delta_{random}}$, referred to as *{random}* here after. Occupancies by Mn and/or Ni ions have been refined for both *4a* and *12d* sites, with an overall occupancy constrained to 100%. Consequently, partial substitution between Ni and Mn was allowed, as reported in [13,18], but no constraint was introduced between the two transition metal sites, allowing to refine the Ni/Mn ratio. Hence, the resulting refined transition metal composition can differ from the starting transition metal ratio. Allowing the oxygen site occupancies to refine did not lead to any significant change from 1.0. Thus,

there was no evidence for anion vacancies in our samples from TOF-PND data and these occupancies were fixed.

Examples of fitted neutron diffraction patterns using the three different APB peak broadening corrections are plotted for $LiMn_{1.58}Ni_{0.42}O_4$ and $LiMn_{1.52}Ni_{0.48}O_4$ prepared at 800°C in S.I.3 and S.I.4 respectively. For all models and samples, the APB peak broadening correction integration strongly improves the refinement. However, careful examinations of selected region highlight subtle differences between these models. For example, comparison of the 1.7-2.6 Å d-spacing region of $LiMn_{1.58}Ni_{0.42}O_4$ prepared at 800°C indicates subtle discrepancies in the fits to the 321 and 332 peaks using the {110} model (Figure 4c). Better fits are obtained using the *{random}* and {100} descriptions (Figure 4a and 4b, respectively). Refinements TOF-PND patterns of $LiMn_{1.52}Ni_{0.48}O_4$ (S.I.5), which exhibits broader Ni/Mn ordering peaks, look equivalent when performed with {100} and {*random*} models while 320 and 411/330 peaks are not well described with the {110} model. Since these differences are subtle, a better comparison between these 3 models can be achieved using the statistical indexes GOF and Rwp.

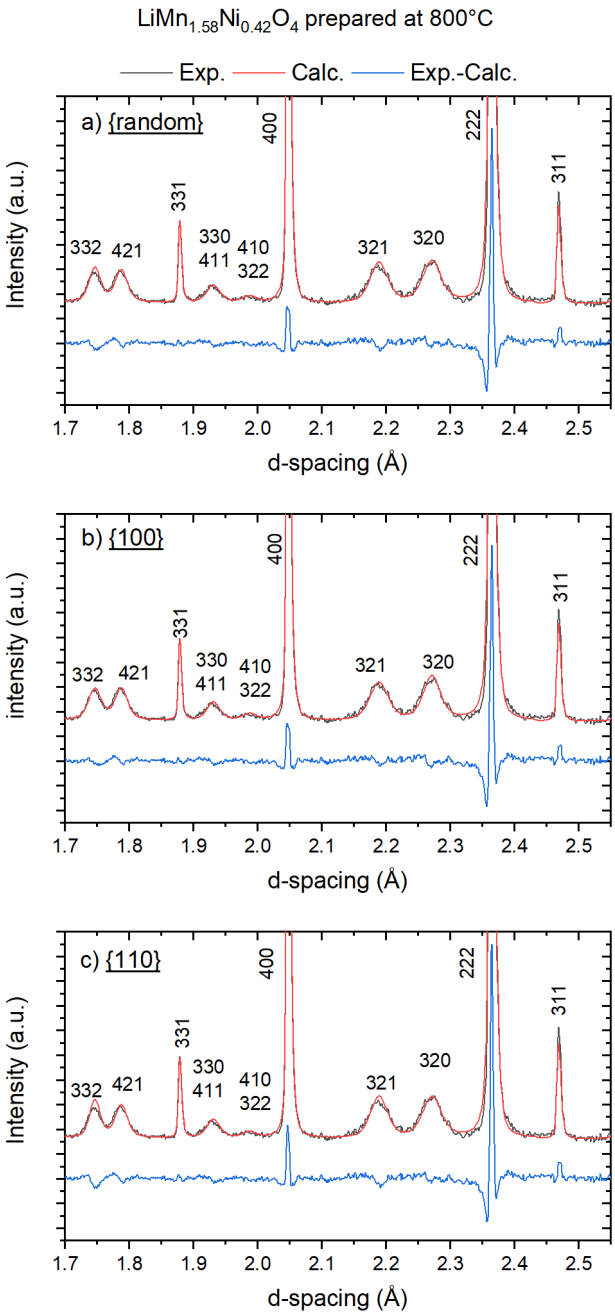

Figure 4: Part of fitted TOF diffraction patterns performed from $LiMn_{1.58}Ni_{0.42}O_4$ sample prepared at 800°C after Rietveld refinements using the 3 APB peak broadening schemes evaluated here: (a) {random}, (b) {100} and (c) {110} APB corrections.

Hence, GOF and Rwp statistical indicators were directly compared to evaluate the three models since each model involves the same number of refined parameters. Indeed, a single parameter is used to describe the APB peak broadening, and only the *hkl* dependence differs between these 3 models. In addition, structural parameters such as atomic positions and cell parameters remain similar for the three models. GOF and Rwp indicators for pairs of models are plotted against one another in Figure 5. Both GOF and Rwp indicate that {100} and *{random}* models are equivalent whatever the sample composition and temperature synthesis (Figure 5a and b). Indeed, most of the points fall with a very small dispersion on the straight line, which indicates equal values. In Figure 5c and d, all the point are below the straight line: the {110} model's statistical indices are lower in all cases and indicate that {100} model produces a better fit than the {110} one.

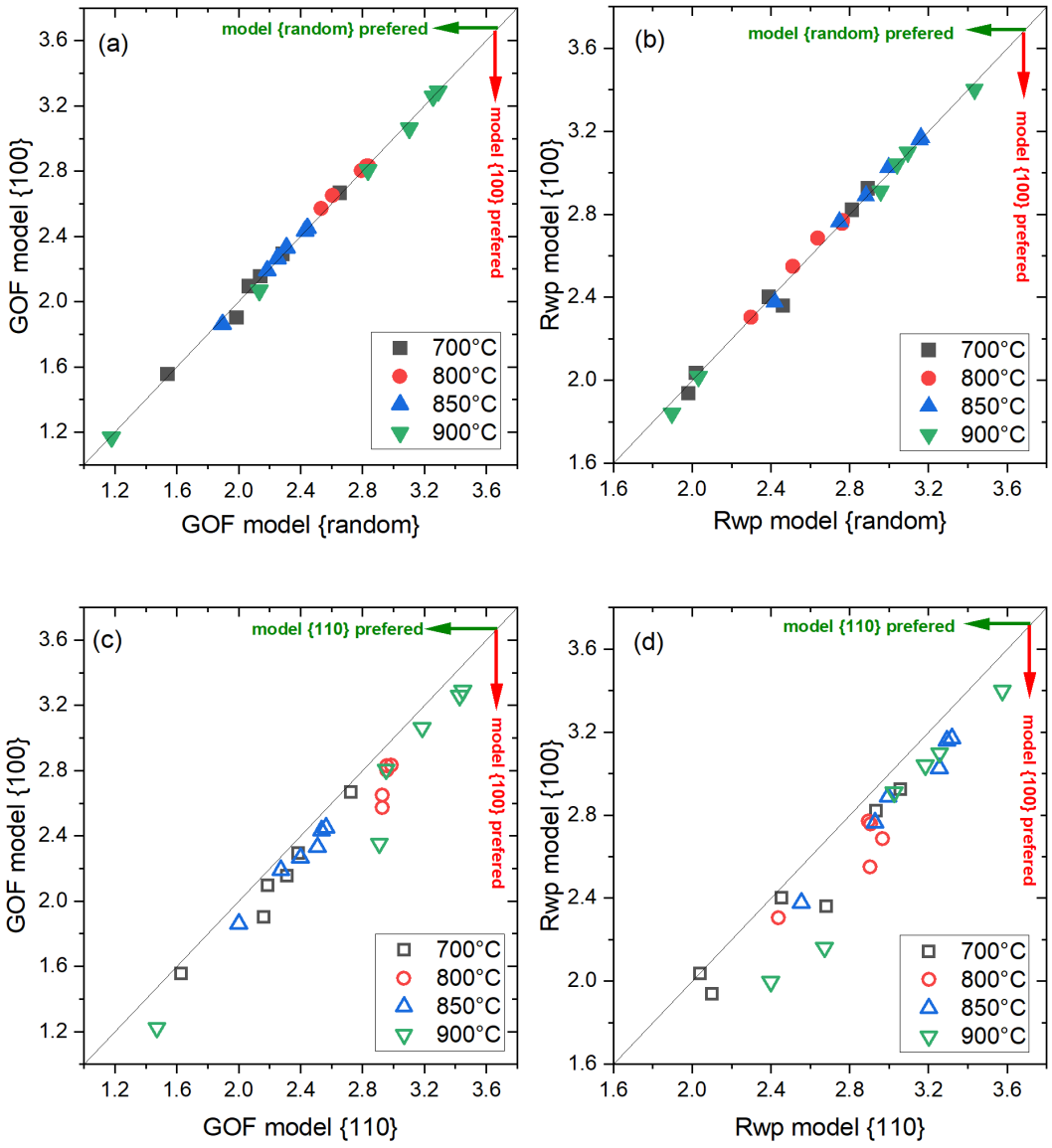

Figure 5: Comparison of Rietveld refinement statistical indicators (a,b) between peak broadening {100} and {random} models and (c,d) between peak broadening {100} and {110} models. ((a) and (c): goodness of fit, (b) and (d): Rwp). (a) and (b) do not show significant differences between {100} and {random} models while (c) and (d) illustrate the improved fit when using the {100} model compared to {110} one.

The {*random*} model, which features independent isotropic domain shape and size within the grain, should be composed of the different allowed types of APB which fulfill the tetrahedral charge invariance rule. Most of the possible APBs lie on the {100} and {110} schemes (which have equal numbers of allowed boundaries) followed by a single possible boundary along {111} planes (between two enantiomorphic structures only) [26]. Then, within the {random} model, APBs delimiting the Ni/Mn ordered domains might be mainly composed of {100} and {110} APB types without figuring a peculiar shape. To get more insight on the APB nature and select the most appropriate correction model, DFT calculations were performed.

Energy calculations of different defect configurations in $LiMn_{1.5}Ni_{0.5}O_4$ using DFT

Since the disorder/defect generation in the Ni/Mn sublattice is directly related to the synthesis temperature increase, energy differences between the ordered ground state ($P4_332$) and various defect configurations of the ideal composition $LiMn_{1.5}Ni_{0.5}O_4$ were performed. For each fully lithiated configuration ($LiMn_{1.5}Ni_{0.5}O_4$), the lithium-free equivalent composition ($Mn_{1.5}Ni_{0.5}O_4$) has been calculated to evaluate the average operating voltage. The lithium electrochemical extraction/insertion reaction of a material $Li_{x1}MO$ can be written as:

$$Li_{x1}MO \rightleftharpoons Li_{x2}MO + (x_1\text{-}x_2)Li \qquad (x_1 > x_2) \qquad (5)$$

According to [57,58], the entropic contributions to the reaction Gibbs energy ΔG_r are small at low temperature, the free energy at 0 K can be used directly. Then, the equilibrium voltage of the cell reaction of equation 5 is given by:

$$\bar{V}(x_1, x_2) \approx -\frac{E\left(Li_{x_1}MO\right) - E\left(Li_{x_2}MO\right) - (x_1 - x_2)E(Li)}{(x_1 - x_2)F} \qquad (6)$$

where $E\left(Li_{x_1}MO\right)$, $E\left(Li_{x_2}MO\right)$ and $E(Li)$ (1.905 eV) are the free energies of $Li_{x1}MO$, $Li_{x2}MO$ and Li, F is the Faraday constant. This evaluation is of utmost importance to ensure a realistic description of the system, since it has been demonstrated that Ni/Mn local ordering impacts the voltage profile [56]. Moreover, several supercells were used depending on the defect/disorder nature. Then, to avoid biased evaluation of the difference energy with the perfectly ordered ground state, the $P4_332$ structure has been adapted and calculated for all the supercells. Table 1 summarizes cell dimensions and *k*-point sampling used for each configuration, cell parameters and free energies for lithiated ($LiMn_{1.5}Ni_{0.5}O_4$) and lithium-free compositions ($Mn_{1.5}Ni_{0.5}O_4$) and the resulting average voltage calculated from these energies. Projection in the *ab*-plane of all the supercells are available in S.I.2. Cell parameters given in Table 1 are those corresponding to the original cubic unit cell and not the supercell. The *random distribution* configuration refers to a randomized distribution of the Mn/Ni ions in a 2 x 2 x 2 supercell while the *partial disorder* features a Mn/Ni repartition in the same cell with respect to the tetrahedral unit charge invariant (S.I.6). Hence, in the latter, the transition metal filled octahedra sequence along <110> direction does not respect the 3 Mn – 1 Ni – 3 Mn… scheme but the tetrahedral units are still composed of 3 MnO_6 and 1 NiO_6 (Figure 1, S.I.6).

For all the configurations, cell parameters of the reduced phase $LiMn_{1.5}Ni_{0.5}O_4$ reach ~8.28 Å instead of ~8.17 Å experimentally [6,8,9]. For the oxidized phase $Mn_{1.5}Ni_{0.5}O_4$, cell parameters of ~8.16 Å are obtained instead of the ~8.00 Å experimental value [6,59]. These overestimations of 1.4% and 2% respectively, are usually observed with GGA+U calculations (~2%) [56,60,61].

The average calculated voltage from the 1 x 1 x 1 *$P4_332$* configuration free energies (eq. (6)) reaches 4.786 V *vs* Li^+/Li, which is in excellent agreement with measured values [8] and previous calculations [56,60,62]. The same local ordering, whatever the supercell size and shape, leads to an average voltage of 4.787 V *vs* Li^+/Li. The energy difference ΔE, which is the difference between the free-energy of a model configuration and the ordered structure free-energy, is used to compare the various configuration. The 2 x 2 x 2 supercell with *random disorder* configuration leads to a significative increase of the free energy compared to the *$P4_332$* configuration, with ΔE = 289.6 meV (27.9 kJ mol^{-1}).

Table 1: Calculated cell dimensions, averaged cell parameters (related to the original $P4_332$ structure), free energies, average voltage potential vs Li^+/Li, and difference of free energy ΔE between the defect/disorder configuration and the ordered structure. All the energies are given per unit formula. [a] partially randomized distribution of Ni/Mn ions in the octahedral sites, the tetrahedral invariant rule is respected. [b] fully random distribution of Ni/Mn ions in the octahedral sites.

Cell dimension (*k-point sampling*)	Configuration		Cell param. (Å)	Free Energy (eV / unit f.)	Average calculated voltage (V)	ΔE (meV / unit f.)
1 x 1 x 1 (*5 x 5 x 5*)	$P4_332$	$LiMn_{1.5}Ni_{0.5}O_4$	8.2819	-45.2221	4.786	
		$Mn_{1.5}Ni_{0.5}O_4$	*8.1618*	*-38.5311*		
2 x 2 x 2 (*3 x 3 x 3*)	$P4_332$	$LiMn_{1.5}Ni_{0.5}O_4$	8.2805	-45.2240	4.787	
		$Mn_{1.5}Ni_{0.5}O_4$	*8.1599*	*-38.5322*		
	Partial disorder [a]	$LiMn_{1.5}Ni_{0.5}O_4$	8.2819	-45.1808	4.748	43.2
		$Mn_{1.5}Ni_{0.5}O_4$	*8.1628*	*-38.5282*		*4.0*
	Random distribution [b]	$LiMn_{1.5}Ni_{0.5}O_4$	8.2938	-44.9344	4.533	289.6
		$Mn_{1.5}Ni_{0.5}O_4$	*8.1574*	-38.4961		*36.1*
$\sqrt{2}$ x $3\sqrt{2}$ x 1 (*3 x 1 x 5*)	$P4_332$	$LiMn_{1.5}Ni_{0.5}O_4$	8.2810	-45.2235	4.787	
		$Mn_{1.5}Ni_{0.5}O_4$	*8.1597*	*-38.5313*		
	APB {110}	$LiMn_{1.5}Ni_{0.5}O_4$	8.2809	-45.2166	4.781	6.9
		$Mn_{1.5}Ni_{0.5}O_4$	*8.1592*	*-38.5308*		*0.5*
4 x 2 x 1 (*1 x 3 x 5*)	$P4_332$	$LiMn_{1.5}Ni_{0.5}O_4$	8.2809	-45.2239	4.787	
		$Mn_{1.5}Ni_{0.5}O_4$	*8.1582*	*-38.5321*		
	APB {100}	$LiMn_{1.5}Ni_{0.5}O_4$	8.2805	-45.2180	4.781	5.9
		$Mn_{1.5}Ni_{0.5}O_4$	*8.1596*	-38.5317		*0.4*

For Li-free cells, the free-energy increase is limited to ΔE = 36.1 meV (3.5 kJ mol^{-1}). It is worth notice that in Li-free cells, all the transition metal ions are in the 4+ oxidation state. The associated calculated average voltage value of 4.533 V *vs* Li^+/Li is far below the experimental one. Hence, the *random disorder* configuration may not be physically realistic due to the large ΔE between lithiated cells and the underestimated cell voltage. The *partial disorder* configuration provides a more probable scenario compared to the *random disorder* since the average cell voltage value (4.748 V *vs* Li^+/Li) remains close to the experimental voltage, and ΔE are limited to 43.2 meV (4.2 kJ mol^{-1}) and 4.0 meV (0.38 kJ mol^{-1}) for lithiated and Li-free cells respectively. These results are consistent with previous reports [56,63]. The {100} and {110} defect configuration energies were computed with 4 x 2 x 1 and $\sqrt{2}$ x $3\sqrt{2}$ x 1 supercells, respectively. In both cases, the average calculated voltage was estimated to 4.781 V *vs* Li^+/Li. Introduction of {100} or {110} defects in $LiMn_{1.5}Ni_{0.5}O_4$ cell leads to limited increase of free energy, with $\Delta E_{\{100\}}$ = 5.9 meV (0.57 kJ mol^{-1}) and $\Delta E_{\{110\}}$ = 6.9 meV (0.67 kJ mol^{-1}), respectively. For Li-free composition $Mn_{1.5}Ni_{0.5}O_4$, introduction of defect has almost no effect on the free energy for both configurations, with $\Delta E_{\{100\}}$ = 0.4 meV (38 J mol^{-1}) and $\Delta E_{\{110\}}$ = 0.5 meV (48 J mol^{-1}). It is worth noticing that the defect density in these supercells is important since the distance between two consecutive defects reaches ~16 Å and 17 Å for {100} and {110}

configurations. Hence, a 3-dimensional distribution of these defects with such high density is sufficient to explain the apparent disordered *Fd-3m* structure. As a result, APB defect formation in $LiMn_{1.5}Ni_{0.5}O_4$ is clearly favoured compared to the *random* distribution scheme or, by a lesser extent, to the *partial disorder*.

Due to the different shape and volume of supercells used to evaluate these defect energies, we expressed their energies in meV.Å^{-2} (mJ.m^{-2}) according to [64]:

$$E_{APB} = \frac{E_{def} - E_{ord.}}{2S} \qquad (5)$$

where E_{def} and $E_{ord.}$ are the free energies of the $LiMn_{1.5}Ni_{0.5}O_4$ supercells with and without the APB defect, S is the surface separating the two domains in the middle of the supercell (S.I.2). Due to the periodicity of supercell, 2 APB are present in each. APB defect energies reach 1.72 meV Å^{-2} (27.6 mJ m^{-2}) and 1.34 meV Å^{-2} (21.5 mJ m^{-2}) for {110} and {100} orientations, respectively. These results deserve several comments. First, for both defect configurations, the very low energy suggests a peculiarly low impact on the local structure at the defect boundary. Hence, the local structure in the vicinity of these defects should not be drastically affected while the *partial order* and *random* configurations are expected to be significantly disturbed. Ni-O and Mn-O bond length distributions in $LiMn_{1.5}Ni_{0.5}O_4$ clearly demonstrate the free-energy / local disorder relation (histogram bin size: 0.01 Å, Figure 6). In the ordered $P4_332$ relaxed structure, Ni^{2+} ions are located in a regular octahedral site with 6 Ni-O bonds of 2.085 Å while Mn^{4+} fill a slightly distorted site, with Mn-O bonds of 1.9618 Å (x2), 1.9349 Å (x2) and 1.9072 Å (x2), in line with experimentally reported values: $d_{Ni\text{-}O}$ = 2.062 Å (x6), $d_{Mn\text{-}O\ (1)}$ = 1.933 Å (x2), $d_{Mn\text{-}O\ (2)}$ = 1.910 Å (x2) and $d_{Mn\text{-}O\ (3)}$ = 1.880 Å (x2) [65]. The bond length differences between Ni-O and Mn-O are coherent with the ionic radii of Mn^{4+} (53 pm) and Ni^{2+} (69 pm) [66]. Introduction of APB defects in these $LiMn_{1.5}Ni_{0.5}O_4$ cells marginally disturbs this distribution as indicated in Figure 6a and 6b. Conversely, if *partial order* scheme spreads bond length distributions with still distinctives Mn-O and Ni-O sets (Figure 6c), the *random* Ni/Mn repartition within the structure yields to an overlap between Ni-O and Mn-O distributions (Figure 6d). In the latter, the spread Mn-O bond length distribution suggests a charge redistribution on the transition metal ions. Longer Mn-O bond lengths (> 2Å) are attributed to the presence of some Mn^{3+}, and conversely, shorter Ni-O bond lengths lie with the presence of Ni^{3+}. The non-respect of the tetrahedron invariance rule is responsive of this charge redistribution. Hence, introduction of APB defects in the structure does not disturb drastically transition metal local environments, which is in line with reports of other groups based on Pair Distribution Function analyses of $LiMn_{1.5}Ni_{0.5}O_4$ samples [19,20]. In a lesser extent, Ni-O and Mn-O bond length distributions of *Random* and *partial disorder* Li-free $Mn_{1.5}Ni_{O.5}O_4$ configurations are disturbed by the defect introduction (Figure S.I.7). Those of {110} and {100} APB model almost overlap with the ordered one. These observations are consistent with the lower free energy differences ΔE reported in Table 1 for Li-free $Mn_{1.5}Ni_{0.5}O_4$ than for the $LiMn_{1.5}Ni_{0.5}O_4$ compositions. This fact is simply explained by the smaller ionic radius difference of Mn^{4+} (53 pm) with Ni^{4+} (48 pm) than with Ni^{2+} (69 pm) [66].

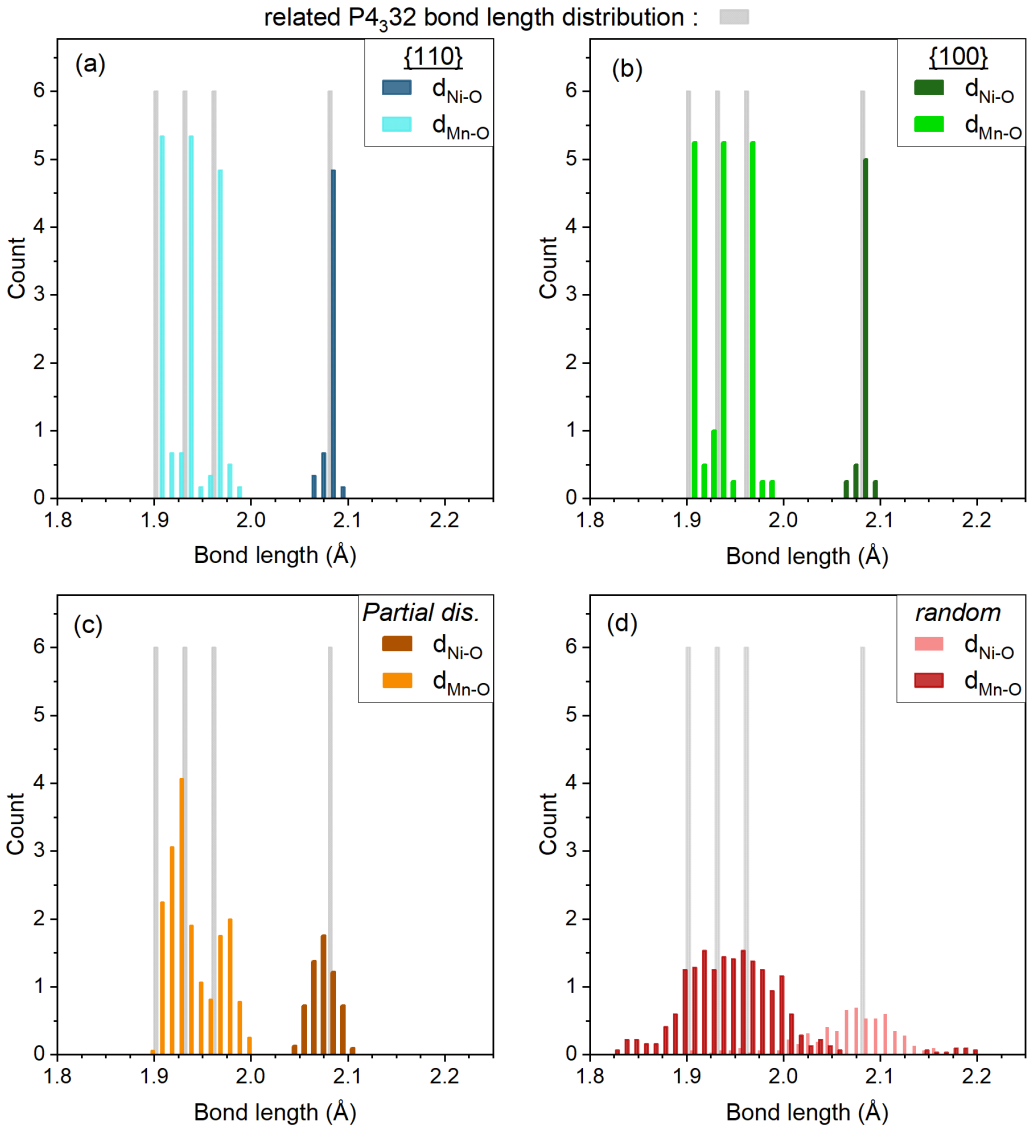

Figure 6: Ni-O and Mn-O bond length distributions in $LiMn_{1.5}Ni_{0.5}O_4$ for (a) {110}, (b) {100}, (c) {Partial dis.} and (d) {random} schemes extracted from DFT calculations. Solid grey bars correspond to the $P4_332$ ordered structure bond length distribution (Bin size: 0.01 Å).

Second, for in $LiMn_{1.5}Ni_{0.5}O_4$, the {100} defect configuration exhibits a slightly lower energy than the {110} one. Between these two configurations, the {100} might be favoured. Neutron diffraction analyses reported in the previous section supports this result, even though the difference between the energies of these two defect configurations is very small. Therefore, the analyses below of cell parameter and APB domain size evolutions with the nickel content and synthesis temperature are performed with the {100} peak broadening correction. It is worth noticing that analyses with {*random*} correction provides similar domain sizes. The {110} scheme has been discarded, due to the overall lower fit quality (Figure 5) and its slightly lower stability from DFT calculations.

$LiMn_{2-x}Ni_xO_4$ spinel compositions and rock salt impurity presence

Increasing the synthesis temperature leads to the presence of a rock-salt type impurity in the samples. Usually, such an impurity is nickel rich and therefore it tends to lower the nickel content of the spinel phase [13,14]. Thus, the refined nickel contents of these spinels were determined from the transition metal site occupancies (structural parameters of all the refinements performed with the {100} model are given in S.I.8 to S.I.11). However, since its composition is still ill defined and subject to discussion, it has been introduced in the refinement procedure in profile matching mode (LeBail method) only with a 2x2x2 supercell of cell parameter of ~8.29 Å [67]. Cell parameters as a function of the refined nickel contents of these spinels are plotted in Figure 7. For all synthesis temperatures, higher nickel contents result in smaller unit cell parameters, and for each temperature the cell parameter evolution vs Ni refined content exhibits an approximately linear behavior. In addition, raising the synthesis temperature for a given nickel refined content induces an increase in the cell parameter. For example, with an initial Ni/Mn ratio of 0.38, the cell parameter increases from 8.1783(5) Å for the sample synthesized at 700°C to 8.1873(5) Å for the sample prepared at 900°C. Such increase is partly attributed to the slightly higher Ni refined content in the 700°C sample compared to sample prepared at higher temperature ($x_{Ni\ 700°C}$ = 0.385(1) and $x_{Ni\ 900°C}$ = 0.377(1)). Moreover, a small amount of oxygen vacancies leads to an increase of Mn^{3+} concentration, which can be responsive of the cell parameter dilation. Hence, a small number of vacancies, not detected by TOF-PND, can be present. For nickel rich samples, the higher nickel content of the $LiMn_{2-x}Ni_xO_4$ solid solution, usually reported as x_{Ni} = 0.5, is never reached, especially for samples prepared at 900°C where the maximum nickel content does not exceed x_{Ni} = ~ 0.45. For temperatures lower than 900°C, there is no evidence of rock-salt impurity in any off the samples and the maximum nickel content is found to come within the range 0.47 and 0.49.

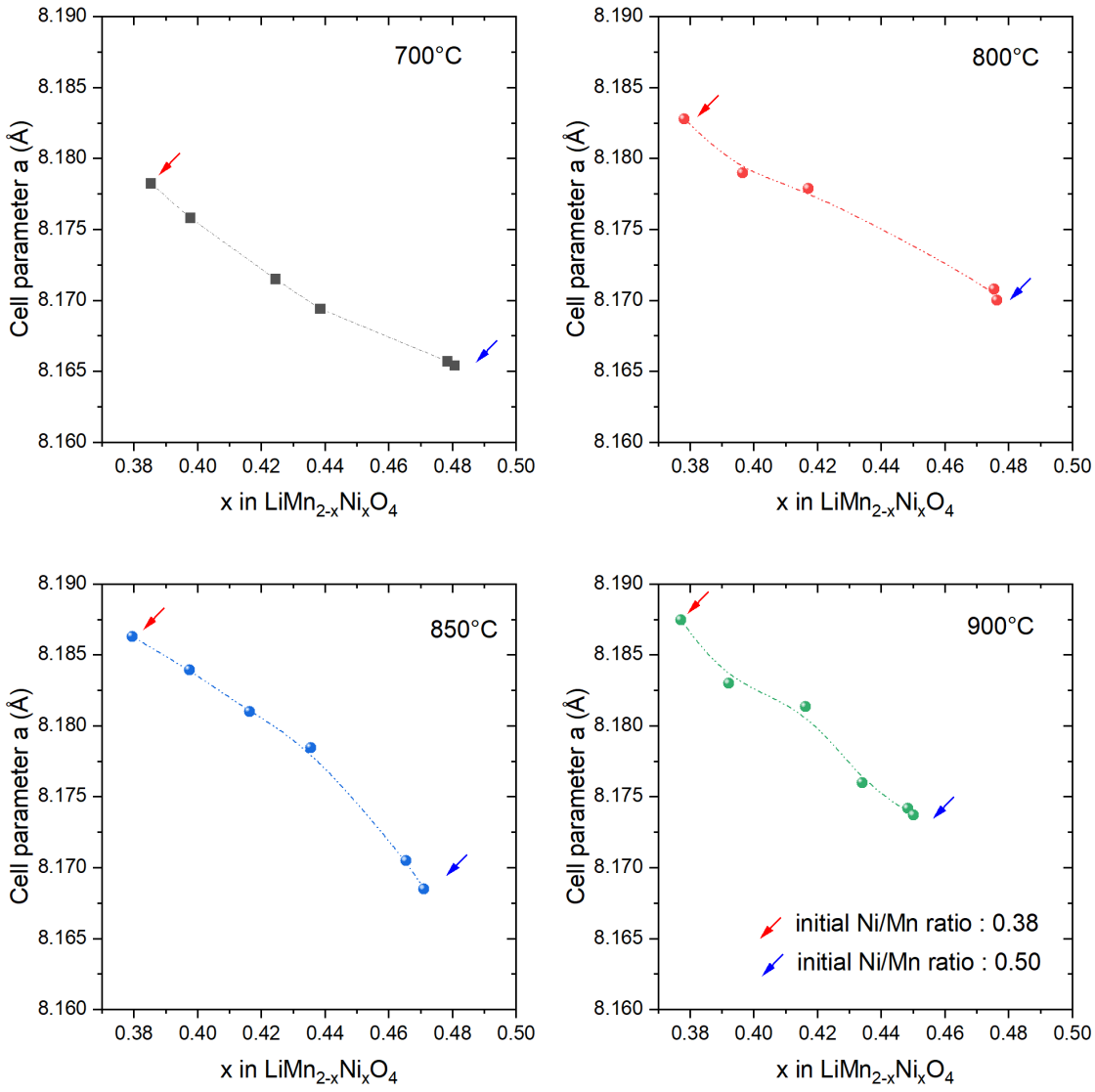

Figure 7: Cell parameter determined from TOF-PND versus refined nickel content extracted from site occupancies of the spinel phase for $LiMn_{2-x}Ni_xO_4$ samples prepared at 700, 800, 850 or 900°C. Red and blue arrows indicate initial Ni/Mn ratio of 0.38 and 0.50, respectively.

Crystallite size and APB domain thickness

A systematic evaluation of the APB domain dimension and particle size has been conducted for all the samples, using the {100} correction. As illustrated in S.I.12, the results show two distinct groups of crystallite sizes. The first group, composed of samples prepared at 800°C and higher, exhibits crystallite sizes larger than 2 µm. It is worth noticing that with these large coherent domains, the sample contribution to the FHMW becomes marginal compared to the instrumental contribution. The second group comprises those prepared at 700°C where the crystallite size does not exceed 250 nm due to a lack of grain growth. SEM images (Figure 2d) presented earlier are in line with these observations.

APB domain mean dimensions as a function of the synthesis temperature and refined nickel compositions of the spinel phase are shown in Figure 8. For 700°C, APB domains growth with the

nickel content, with a maximum of 109 nm reached for the richest composition obtained $LiMn_{1.519(1)}Ni_{0.481(1)}O_4$, which is similar of the same order of magnitude than the mean crystallite size (114 nm). As a result, for a synthesis temperature of 700°C, the Ni/Mn ordered domain size for the Ni-richest composition is mainly limited by the mean crystallite size and the absence of grains growth. Interestingly, lower is the nickel content, lower is the APB domain size, while the mean crystallite sizes fluctuate between 80 to 180 nm. The APB domain thickness, with a minimum of 13.0(5) nm for $LiMn_{1.615(1)}Ni_{0.385(1)}O_4$ increases linearly with the nickel content.

Compared to the Ni/Mn mean domain thickness evolution of samples prepared at 700°C, the APB domain size evolution for samples prepared at temperature of 800°C and higher, is drastically different. For 800°C and 850°C, similar trends are observed for APB domain size evolution versus refined spinel nickel content. APB domain sizes observed in the composition with lowest x, $LiMn_{1.62}Ni_{0.38}O_4$, are 16 and 9 nm for synthesis temperatures of 800°C and 850°C respectively. The mean size then gradually increases with the nickel content to reach a maximum around x_{Ni} = ~0.44 of 28 nm before decreasing down to 4 nm (800°C) and 3 nm (850°C). A similar trend is observed for 900°C samples with smaller domain sizes and diminution of the maximum nickel content, due to the nickel rich rock-salt impurities. As a result, the maximum APB domain thickness is observed for $LiMn_{1.584(6)}Ni_{0.416(6)}O_4$ with 20 nm. The lowest value, determined in $LiMn_{1.547(7)}Ni_{0.453(7)}O_4$ (the richest nickel composition), is approximately 2.5 nm.

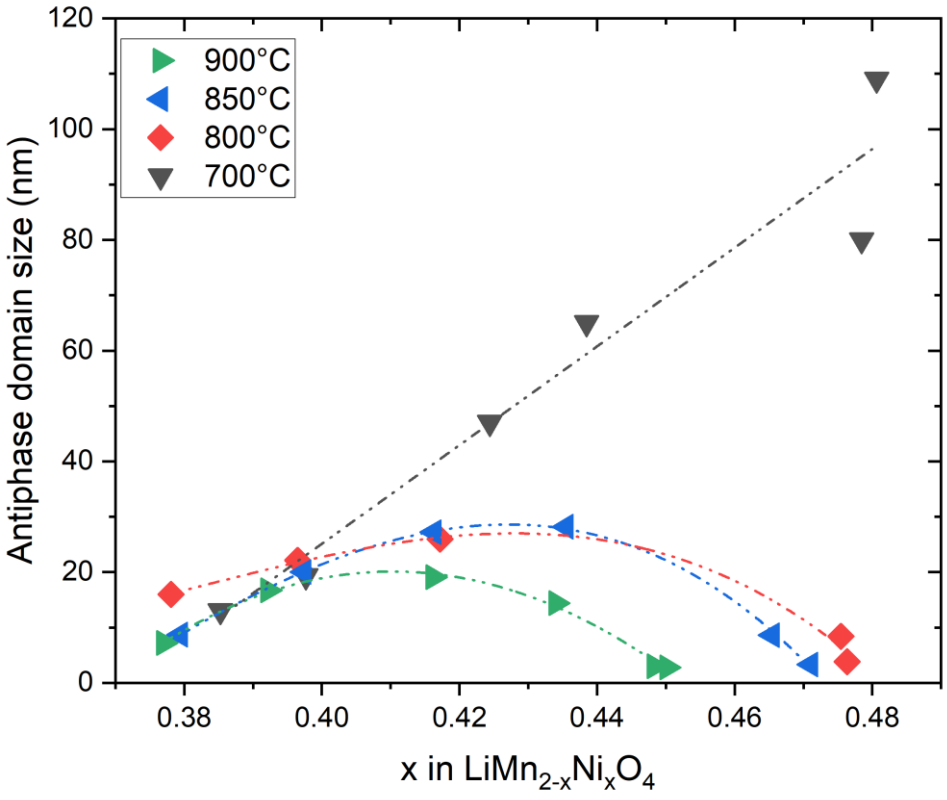

Figure 8: APB mean domain size extracted from the TOF neutron data Rietveld refinement as a function of the refined spinel phase refined nickel content for several synthesis temperatures (2 successive thermal treatments of 48h with an intermediate grinding). Dash-dot lines are guide for the eyes.

The general trend observed for samples prepared at 800°C and higher raises several points. First, a domain size maximum is systematically observed slightly below the maximum nickel content in the spinel, between x_{Ni} = ~0.41 at 900°C to x_{Ni} = ~0.435 at 800°C. Second, close to the Ni-rich limit, the

Ni/Mn ordered domain size decreases. It is attributed to the oxygen losses which lead to the formation of the rock-salt impurity. As mentioned earlier, rock-salt impurity was detected only for few samples, one prepared at 850°C and 2 prepared at 900°C (S.I.10 and 11). The reduction of the maximum nickel content observed ($LiMn_{1.524(2)}Ni_{0.476(2)}O_4$ at 800°C, $LiMn_{1.531(1)}Ni_{0.469(1)}O_4$ at 850°C, $LiMn_{1.552(2)}Ni_{0.448(2)}O_4$ at 900°C) is due to this rock-salt impurity formation. Hence, this equilibrium between the spinel and the rock salt phases probably facilitates the APB formation due to the local reorganization induced by the Ni ions migration. Last, below x_{Ni} = 0.41-0.43, the domain sizes gradually decrease, probably due to the ability of the system to break the Ni/Mn overall ordering without violation of the tetrahedral charge invariance [55].

Influence on the electrochemical properties

Figure 9a and 9b show the 5th cycle oxidation curves of $LiMn_{1.5}Ni_{0.5}O_4$ and $LiMn_{1.6}Ni_{0.4}O_4$. In both plots, a contribution at 4.0-4.1 V is observed followed by two successive voltage plateaus in the 4.67 - 4.80 V narrow voltage window. The 4.0-4.1 V contribution is related to the Mn^{3+}/Mn^{4+} redox couple and indicates the presence of Mn^{3+} ions presence in the reduced electrode ($Li_1Mn_{2-x}Ni_xO_4$). The evolution of the Mn^{3+}/Mn^{4+} contribution to the faradaic yield, i.e., the Mn^{3+} fraction, is reported in Figure 9c. In addition, from the chemical composition, Mn^{3+} expected contribution to the faradaic yield in $LiMn_{2-x}Ni_xO_4$ is defined as $f_{Mn^{3+}}(\%) = 100(1-2x)$. Hence, based on neutron diffraction refinements presented above and assuming a stoichiometric amount of oxygen, Mn^{3+} contribution was evaluated and is presented in Figure 9c for comparison. For $LiMn_{1.5}Ni_{0.5}O_4$ initial composition samples, both electrochemical measurements and neutron diffraction exhibit the same trend with similar values. From TOF-PND analysis, the Mn^{3+} fraction is calculated to be 3.9 % for the 700°C sample and increases to 10.3 % for the 900°C sample. These values are in excellent agreement with those extracted from galvanostatic oxidation curves, reaching 2.3 and 10.7 %, respectively. Then, for such starting composition, resulting products may not contain a significant amount of oxygen vacancies and the Mn^{3+} content is attributed to the lower nickel solubility in the spinel phase at higher temperature. As a result, the weight loss reported elsewhere for the $LiMn_{1.5}Mn_{0.5}O_4$ initial composition is attributed to the rock-salt phase impurity formation, which implies oxygen losses when obtained from a spinel phase [68,69]. The behavior of $LiMn_{1.6}Ni_{0.4}O_4$ initial composition samples is slightly different. From electrochemical measurements, an ill-defined trend suggests a stable Mn^{3+} fraction of around 23% excepted for the 700°C sample which shows a slightly lower Mn^{3+} content (~19%). From TOF-PND, whatever the temperature, the Mn^{3+} content remains constant, at a mean value of 20-21%. Both experimental techniques show similar Mn^{3+} content for all synthesis temperatures. However, few oxygen vacancies are possibly present for samples prepared at 800°C and higher, according to the 4 % Mn^{3+} fraction increase observed compared to the sample prepared at 700°C.

As already reported by Casas-Cabanas *et al* [17], the voltage difference ΔE between the two plateaus is affected by the presence of APB defects. Figure 9d shows the voltage differences as a function of the synthesis temperature for $LiMn_{1.5}Ni_{0.5}O_4$ and $LiMn_{1.6}Ni_{0.4}O_4$ initial compositions. As evidenced for $LiMn_{1.5}Ni_{0.5}O_4$ initial composition (Figure 9a), larger defect concentration result in higher ΔE. Hence, two voltage plateaus, with a narrow ΔE of 15mV, are observed for the 700°C sample while the 900°C sample exhibits a clear ΔE of ~54 mV. This might be correlated to the increasing disorder in the structure by raising the defect concentration (reduction of the average APB domain size) and the Mn^{3+} ions content increases, induced by the lower nickel solubility for high synthesis temperatures. The substitution of a nickel ion in a tetrahedral unit by a manganese induces local distortion and disorder, due to a charge redistribution on the surrounding Mn ions. On the contrary, the voltage difference ΔE all the $LiMn_{1.6}Mn_{0.4}O_4$ samples prepared at different

temperatures remain in the ~28 – 37 mV range and is not drastically affected. As can be seen in Figure 8, the APB domain sizes are almost identical for all synthesis temperatures and the Ni/Mn ratio in the spinel does not vary significantly. Only the Mn^{3+} ions content evolves slightly for the $LiMn_{1.6}Ni_{0.4}O_4$ (Figure 9c), in good accordance with the limited ΔE variation observed in Figure 9d.

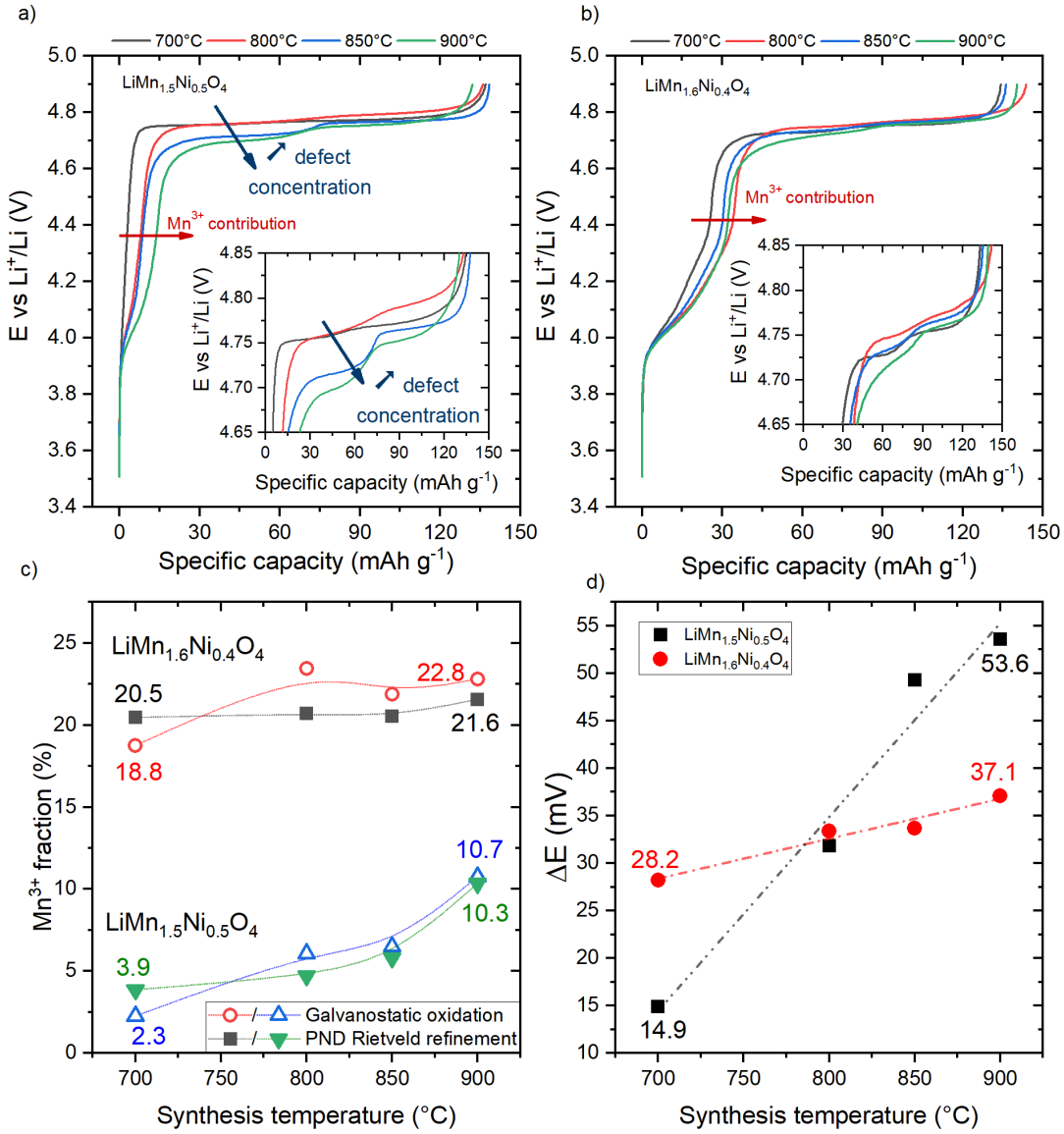

Figure 9: Galvanostatic oxidation curves recorded at C/10 rate of (a) $LiMn_{1.5}Ni_{0.5}O_4$ and (b) $LiMn_{1.6}Ni_{0.4}O_4$ samples prepared at various temperatures. (c) Mn^{3+} fraction in $LiMn_{1.6}Ni_{0.4}O_4$ and $LiMn_{1.5}Ni_{0.5}O_4$ samples determined from the galvanostatic curve (open symbol) and the TOF-PND Rietveld refienement (solid symbol). (d) voltage difference ΔE between Ni^{2+}/Ni^{3+} and Ni^{3+}/Ni^{4+} plateaus of $LiMn_{1.5}Ni_{0.5}O_4$ (black square) and $LiMn_{1.6}Ni_{0.4}O_4$ (red dot) prepared at various temperatures.

14 days annealing at 700°C of 900°C $LiMn_{1.5}Ni_{0.5}O_4$ sample

The $LiMn_{1.5}Ni_{0.5}O_4$ sample prepared at 900°C and analyzed in the above sections has been subsequently annealed at 700°C for two weeks. TOF-PND pattern collected for this sample indicates a clear ordering of the Ni/Mn sublattice according to the *$P4_332$* space group and the Rietveld refinement within the *{100}* defect scheme leads to a large APB domain size of ~360 nm (Figure 10a). Hence, thanks to the production of micrometer-sized crystallites during the 900°C synthesis process

(see Figure 2d), further annealing at 700°C serves to increase the size of Ni/Mn long range ordered domains by a factor 3 compared to the direct synthesis at 700°C (APB domain size of 80-100 nm for 700°C sample). In addition, no trace of the rock-salt impurity was evidenced and the refined nickel content in the spinel phase is higher than that of the original 900°C sample, close to the precursor Ni/Mn ratio (0.495 compared to 0.448). Hence, the nickel-rich rock-salt impurity formation from the spinel phase appears to be reversible with an annealing at appropriate temperature. These results are supported by the electrochemical curves displayed in Figure 10b. Specific capacities exhibited by the 700°C sample and the 900°C sample one annealed at 700°C are both the same, 137 mA h g^{-1}, with a quasi-overlap of the galvanostatic curves. This contrasts with a lower specific capacity for the unannealed 900°C sample of only 131.7 mA h g-1 which we attribute to the weight penalty of the rock-salt impurity. In addition, the 900°C sample exhibits two well separate plateaus at 4.7 and 4.75 V *vs* Li^+/Li and a contribution at 4-4.1 V due to Mn^{3+}/Mn^{4+} redox couple contribution.

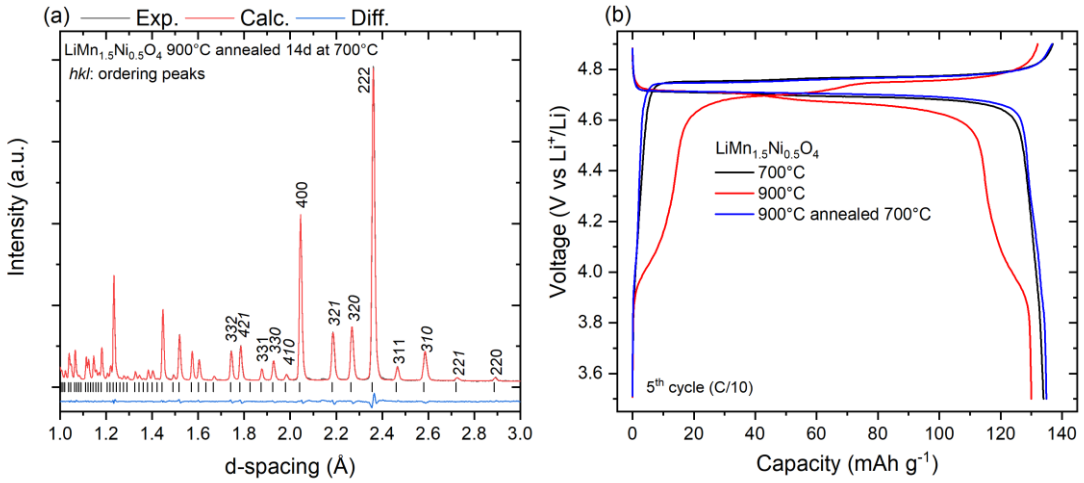

Figure 10: (a) Fitted TOF-PND pattern $LiMn_{1.5}Ni_{0.5}O_4$ sample prepared at 900°C and annealed 14 days at 700°C. (b) comparison of the galvanostatic curves of 700°C, 900°C and 900°C annealed 700°C $LiMn_{1.5}Mn_{1.5}O_4$ sample.

Conclusions

To summarize, using TOF-PND experiments we have been able to observe and characterize domains of Ni/Mn ordering in the nickel-rich part of the $LiMn_{2-x}Ni_xO_4$ solid solution ($0.38 \leq x \leq 0.50$), retained to room temperature even in samples synthesized at 900°C. These Ni/Mn ordered domains, smaller than the overall crystallite size, are separated by antiphase domain boundaries (APB). Diffraction peaks with *hkl* indexes of mixed parity and whose intensity contributions only come from the Ni/Mn order, exhibit a broadening related to the APB density in the crystallite. Hence, the TOF-PND data set has been analyzed as a single ordered spinel structure within the $P4_332$ space group, and an additional parameter representing the probability of crossing an antiphase domain boundary used to model the peak broadening. According to previous studies on $LiMn_{1.5}Ni_{0.5}O_4$ [56] and on the isostructural phase $Li_{0.5}Fe_{2.5}O_4$ [55], APB boundary must be conservative, i.e. in $LiMn_{2-x}Ni_xO_4$ phases two adjacent Ni-filled octahedra are not allowed. Then, based on the *hkl*-dependent peak broadening models developed in [26], we demonstrate that the preferred direction for conservative APB propagation is along {100} planes rather than {110} planes. The random orientation scheme cannot be discounted from the TOF-PND structure models since it provides similar agreement factors to the {100} configuration. However, the conservative condition is needed.

DFT calculations performed in this work support the absence of adjacent NiO_6 octahedrons claimed elsewhere [56,63]: a random Ni/Mn distribution into the occupied octahedrons of the structure leads to a large increase of the free energy, of +289.6 meV / f.u. (27.9 kJ mol^{-1}) compared to the ordered structure, while a partial disorder, respecting the tetrahedral charge invariance, limits this augmentation to 43.2 meV / f.u. (4.2 kJ mol^{-1}). Moreover, the introduction of {100} and {110} conservative APB defects in supercells (4 x 2 x 1 and $\sqrt{2}$ x $3\sqrt{2}$ x 1 respectively) does not affect significatively the free energy of the system: these planar defects lead to a free energy increase of 1.34 meV $Å^{-2}$ (21.5 mJ m^{-2}) and 1.72 meV $Å^{-2}$ (27.6 mJ m^{-2}) for {100} and {110} orientations respectively. Thus, these defects are responsible for the apparent disorder often reported for samples prepared at 900°C [6,13]. Although only having a small energy difference compared to the {110} configuration, the {100} orientation is preferred, in agreement with TOF-PND experimental results. Furthermore, the influence of these planar defects on the local structure of DFT relaxed cells, through the Ni-O and Mn-O bond length distributions, has been analysed. {100} or {110} APB defect introduction does not significantly disturb the Ni-O/Mn-O bond length distributions, while random and partly disordered schemes spread them. This result supports an APB driven apparent disorder evidenced here and the local ordering observed elsewhere from neutron PDF studies [19,20].

The coherence length of these ordered domains, and therefore the APB defect density, is mainly affected by two factors: the synthesis temperature, and the nickel content. For x > 0.40, increasing the synthesis temperature leads to an increase of the defect density for each composition. For synthesis temperatures of 800°C and above, the defect density has a marked dependence on the nickel content. The larger coherent domains are observed in the middle of the composition range studied, for x~0.43-0.44 in $LiMn_{2-x}Ni_xO_4$. For lower or higher x values, the sizes of the ordered domain decrease, with the smallest value of ~2.5 nm observed for $LiMn_{1.55(1)}Ni_{0.45(1)}O_4$ prepared at 900°C. In the latter sample, refined transition metal composition differs from the initial Ni/Mn ratio (1/3), due to the formation of the nickel-rich rock-salt impurity. This behavior is clear in the Ni-rich part of the phase diagram (x > 0.44) where increasing the synthesis temperature lowers the nickel content in the spinel phase. In addition, the refined compositions from TOF-PND data of our $LiMn_{2-x}Ni_xO_4$ samples with initial x=0.50 prepared at various temperatures imply the confirm the presence of a fraction Mn^{3+} which are in good accordance with the Mn^{3+}/Mn^{4+} redox couple contribution determined from galvanostatic curves. These results comfort the lowering of the nickel content with the synthesis temperature in similar proportion and rule out the presence of oxygen vacancies in our synthesis conditions.

Supporting Information

Representation of the 8 possible cells; *ab*-plane projections of the supercells used for DFT calculations with defect position; Fitted TOF diffraction patterns performed from $LiMn_{1.58}Ni_{0.42}O_4$ and $LiMn_{1.52}Ni_{0.48}O_4$ samples prepared at 800°C after Rietveld refinements using 3 APB peak broadening schemes: {100}, {110} or {random} APB corrections; Part of fitted TOF diffraction patterns performed from $LiMn_{1.58}Ni_{0.42}O_4$ sample prepared at 800°C after Rietveld refinements using the 3 APB peak broadening schemes; 2 x 2 x 2 supercell for random Ni / Mn distribution and partial disorder respecting the tetrahedral charge invariance principle; Ni-O and Mn-O bond length distributions in $Mn_{1.5}Ni_{0.5}O_4$ for {110}, {100}, {Partial disorder} or {random distribution} schemes extracted from DFT calculations; Crystallographic Data and Atomic Positions of $LiMn_{2-x}Ni_xO_4$ samples prepared at 700,

800, 850 or 900°C deduced from their Rietveld Refinements of TOF-PND Diffraction Patterns; Mean particle size estimated from TOF-neutron diffraction patterns.

Acknowledgements

Experiments on GEM (Xpress Access XB1890379/80, XB1990085/86/87) and Polaris (Proposal RB 1920335) at the ISIS Pulsed Neutron and Muon Source were supported by a beam time allocation from the Science and Technology Facilities Council. Financial supports from ANR project « CASSIOPES » N°17-CE09-0016-03 and UPE (Université Paris Est) are acknowledged. Dr. Sandrine Tusseau-Nenez (DIFFRAX, Ecole Polytechnique, Palaiseau) and Dr. Marie-Noëlle de Noirfontaine (LSI, Ecole Polytechnique, Palaiseau) are acknowledge for valuable discussions around Topas software.

References:

[1] G. Q. Liu, L. Wen, Y. M. Liu, Spinel $LiNi_{0.5}Mn_{1.5}O_4$ and its derivatives as cathodes for high-voltage Li-ion batteries, J. Solid State Electrochem. 14 (2010)2191–2202

[2] W. Li, B. Song, A. Manthiram, High-voltage positive electrode materials for lithium-ion batteries, *Chem. Soc. Rev.* 46 (2017) 3006-3059

[3] W. Choi, A. Manthiram, Comparison of Metal Ion Dissolutions from Lithium-Ion Battery Cathodes, *J. ElectroChem. Soc.* 153 (2006) A1760-A1764

[4] J.-H. Kim, N.P.W. Pieczonka, L. Yang, Challenges and Approaches for High-Voltage Spinel Lithium-Ion Batteries, *Chem. Phys. Chem.*, 15 (2014) 1940-1954

[5] O.K. Park, Y. Cho, S. Lee, H.-C. Yoo, H.-K. Song, J. Cho, Who will drive electric vehicles, olivine or spinel?, *Energy Environ. Sci.* 4 (2011) 1621-1633

[6] Manthiram, A.; Chemelewski K.; Lee, E.-S.; A perspective on the high-voltage $LiMn_{1.5}Ni_{0.5}O_4$ spinel cathode for lithium-ion, *Energy Environ. Sci*., **2014**, *7*, 1339-1350

[7] Kunduraci, M.; Amatucci, G.G.; The effect of particle size and morphology on the rate capability of 4.7V $LiMn_{1.5+d}Ni_{0.5-d}O_4$ spinel lithium-ion battery cathodes, *electrochim. Acta*, **2008**, *53*, 4193-4199

[8] Ariyoshi, K.; Iwakoshi, Y.; Nakayama, N.; Ohzuku, T.; Topotactic two-phase reactions of $Li[Ni_{1/2}Mn_{3/2}]O_4$ ($P4_332$), *J. Electrochem. Soc.* **2004**, *151*, A296-A303

[9] Kim, J.-H.; Myung, S.-T.; Yoon, C. S.; Kang, S. G.; Sun, Y.-K.; Comparative study of $LiNi_{0.5}Mn_{1.5}O_{4-\delta}$ and $LiNi_{0.5}Mn_{1.5}O_4$ cathodes having two crystallographic structures: Fd-3m and $P4_332$, *Chem. Mater.* **2004**, *16,* 906-914.

[10] Liu, D.; Zhu, W.; Trottier, J.; Gagnon, C.; Barray, F.; Guerfi, A.; Mauger, A.; Groult, H.; Julien, C.M.; Goodenough, J.B.; Zaghib, K.; Spinel materials for high-voltage cathode in Li-ion batteries, *RSC Adv.* **2014**, *4*, 154-167

[11] Ma, X.; Kang, B.; Ceder, G.; High rate micron-sized ordered $LiNi_{0.5}Mn_{1.5}O_4$, *J. Electrochem. Soc.* **2010**, *157*, A925-A931

[12] Kunduraci, M.; Amatucci, G.G.; Effect of oxygen non-stoichiometry and temperature on cation ordering in $LiMn_{2-x}Ni_xO_4$ ($0.50 \geq x \geq 0.36$) spinels, *J. Power Sources*, **2007**, *165*, 359-367

[13] Cabana, J.; Casas-Cabanas, M.; Omenya, F.O.; Chernova, N.A.; Zeng, D.; Whittingham, M. S.; Grey, C.P.; Composition-structure relationships in the Li-ion battery electrode material $LiNi_{0.5}Mn_{1.5}O_4$, *Chem. Mater*. **2012**, *24*, 2952-2964

[14] Zhong, Q.; Bonakdarpour, A.; Zhang, M.; Gao, Y.; Dahn, J. R.; Synthesis and electrochemistry of $LiNi_xMn_{2-x}O_4$, *j. Electrochem. Soc.* **1997**, *144*, 205-213

[15] Pasero, D.; Reeves, N.; Pralong, V.; West, A.; Oxygen nonstoichiometry and phase transition in $LiMn_{1.5}Ni_{0.5}O_{4-\delta}$, *J. Electrochem. Soc.*, **2008**, *155*, A282-A291

[16] Gryffoy, D.; Vandenberghe, R.E; Legrand, E.; A neutron diffraction study of some spinel compounds containing octahedral Ni and Mn at 1:3 ratio, *Mat. Sci. Forum* **1991**, *79-82*, 785-790

[17] Casas-Cabanas, M.; Kim, C.; Rodriguez-Carvajal, J.; Cabana, J.; Atomic defects during ordering transitions in $LiNi_{0.5}Mn_{1.5}O_4$ and their relationship with electrochemical properties, *J. Mater. Chem. A*, **2016**, *4*, 8255-8262

[18] Kim, J.-H.; Huq, A.; Chi, M.; Pieczonka, N. P.W.; Lee, E.; Bridges, C.A.; Tessema, M.M.; Manthiram, A.; Persson, K.A.; Powell, B.R.; Integrated nano-domains of disordered and ordered spinel phases in $liNi_{0.5}Mn_{1.5}O_4$ for Li-ion batteries, *Chem. Mater.* **2014**, *26*, 4377-4386

[19] Liu, J.; Huq, A.; Moorhead-Rosenberg, Z.; Manthiram, A.; Page, K.; Nanoscale Ni/Mn ordering in the high voltage spinel cathode $LiNi_{0.5}Mn_{1.5}O_4$, *Chem. Mater.* **2016**, *28*, 6817-6821
[20] Chen, Y.; Cheng, Y.; Li, J.; Feygenson, M.; Heller, W.T.; Liang, C.; An, K.; Lattice-cell orientation disorder in complex oxides, *Adv. Energy Mater.* **2016** 1601950/1-9
[21] Sears, V. F.; Neutron scattering lengths and cross sections, *Neutron News*, **1992**, *3*, 26-37
[22] Scardi, P.; Leoni, M.; Diffraction whole-pattern modelling study of anti-phase domains in Cu_3Au, *Acta Mat.* **2005**, *53*, 5229-5239
[23] Leoni, M.; Whole powder pattern modelling: microstructure determination from powder diffraction data, In *International Tables for Crystallography Vol. H: Powder diffraction*, Willey, 2019; pp. 288–303. DOI: 10.1107/97809553602060000951
[24] Heisig, T.; Kler, J.; Du, H.; Baeumer, C.; Hensling, F.; Glöß, M.; Moors, M.; Locatelli, A.; Onur Menteş, T.; Genuzio, F.; Mayer, J.; De Souza, R. A.; Dittmann, R.; Antiphase boundaries constitute fast cation diffusion paths in $SrTiO_3$ memristive devices, *Adv. Funct. Mater.***2020**, *30*, 2004118/1-8
[25] Lindén, J.; Karppinen, M.; Shimada, T.; Yasukawa, Y.; Yamauchi, H.; Observation of antiphase boundaries in Sr_2FeMoO_6. *Phys. Rev. B* **2003**, *68*, 174415/1-5
[26] Cheary, R.W.; Grimes, N.W.; Investigation of antiphase domains in lithium ferrite by analysis of the broadened X-ray diffraction lines, *acta Cryst.* **1978**, *A34*, 74-84
[27] Portier, R.; Lefebvre, S.; Fayard, M.; Lejus, A.M.; Enantiomorphous domains in stoechiometric lithium aluminate $LiAl_5O_8$, *Mat. Res. Bull.* **1975**, *10*, 883-888
[28] Lefevbre, S.; Portier, R.; Fayard, M.; Structure en domaines de l'oxyde non centrosymétrique $LiFe_5O_8$, *Phys. Stat. Sol.* **1974**, *24*, 79-88
[29] Wilson, A.J.C.; Zsoldos, L.; The reflexion of X-rays from the 'anti-phase nuclei' of $AuCu_3$. II, *Proc. R. Soc. Lond. A* **1966**, *290*, 508–514
[30] Warren, B.E.; X-ray diffraction, 2nd ed. New York (NY): Dover 1990
[31] Shin, D. W.; Bridges, C. A.; Huq, A.; Patanthaman, M. P.; Manthiram, A.; Role of cation ordering and surface segregation in high-voltage spinel $LiMn_{1.5}Ni_{0.5-x}M_xO_4$ (M = Cr, Fe, and Ga) cathodes for lithium-ion batteries, *Chem. Mater.* **2012**, *24*, 3720-3731
[32] Wagemaker, M.; Ooms, F.G.B.; Kelder, E. M.; Schoonman, J.; Kearley, G. J.; Mulder, F. M.; Extensive migration of ordered $LiMg_{0.1}Ni_{0.4}Mn_{1.5}O_4$ spinel, *J. Am. Chem. Soc.* **2004**, *126*, 13526-13533
[33] Liu, D.; Han, J.; Goodenough, J.B.; Structure, morphology, and cathode performance of $Li_{1-x}[Ni_{0.5}Mn_{1.5}]O_4$ prepared by coprecipitation with oxalic acid, *J. Power Sources*, **2010**, *195*, 2918–2923
[34] Hannon, A. C.; Results on disordered materials from the GEneral Materials diffractometer, GEM, at ISIS, *Nucl. Instrum, Methods Phys. Res. Sect. A* **2005**, *551*, 88-107
[35] Emery, N.; **2019**: STFC ISIS Neutron and Muon Source, https://doi.org/10.5286/ISIS.E.RB1990085-1
[36] Emery, N.; **2019**: STFC ISIS Neutron and Muon Source, https://doi.org/10.5286/ISIS.E.RB1990086-1
[37] Emery, N.; **2019**: STFC ISIS Neutron and Muon Source, https://doi.org/10.5286/ISIS.E.RB1990087-1
[38] Emery, N.; **2019**: STFC ISIS Neutron and Muon Source, https://doi.org/10.5286/ISIS.E.RB1890379-1
[39] Emery, N.; **2019**: STFC ISIS Neutron and Muon Source, https://doi.org/10.5286/ISIS.E.RB1890380-1
[40] Smith, R. I.; Hull, S.; Tucker, M. G.; Playford, H. Y.; McPhail, D. J.; Waller, S. P.; Norberg, S. T.; The upgraded Polaris powder diffractometer at the ISIS neutron source, *Rev. Sci. Instrum.* **2019**, *90,* 115101
[41] Emery, N.; Smith, R.I.; Bathia, A.; Baddour-Hadjean, R.; **2019** Cation ordering exploration in Ni rich part of the solid solution $LiNi_xMn_{2-x}O_4$ spinels as a function of the synthesis temperature, STFC ISIS Neutron and Muon Source, https://doi.org/10.5286/ISIS.E.RB1920335
[42] Larson, A. C.; Von Dreele, R. B.; General Structure Analysis System (GSAS), Los Alamos National Laboratory, Technical Report N°. LAUR86-748, **2004**
[43] Toby, B.; EXPGUI, a graphical user interface for GSAS, *J. Appl. Cryst.* **2001**, *34*, 210-213
[44] Diffrac^{plus} TOPAS v4.2, BRUKER-AXS GmbH: Karlsrhe, Germany, **2009**.
[45] Evans, J. S. O.; Advanced input files & parametric quantitative analysis using topas, *Mat. Sci. Forum* **2010**, *651,* 1-9
[46] Topas Wiki, URL:http://topas.dur.ac.uk/ (accessed 15/03/2022)
[47] Dinnebier, R. E.; Leineweber, A.; Evans, J.S.O.; Rietveld Refinement: practical powder diffraction pattern analysis using TOPAS, **2019**, Ed. De Gruyter, ISBN 978-3-11-045621-9
[48] Kresse, G.; Firthmüller, J.; Efficient iterative sschemes for *Ab-initio* total-energy calculation using plane-wave basis set, *Phys. Rev. B: Condens. Matter Mater. Phys.* **1996**, *54*, 11159-11186
[49] Blochl, P.E.; Projector augmented-wave method, *Phys. Rev. B: Condens. Matter Mater. Phys.* **1994**, *50*, 17953-17979

[50] Perdew, J.P.; Jackson, K.A.; Pederson, M.R.; Singh, D.J.; Fiolhais, C.; Atoms, molecules, solids and surfaces: applications of the generalized gradient approximation for exchange-correlation, *Phys. Rev. B: Condens. Matter Mater. Phys.* **1992**, *46*, 6671-6687

[51] Perdew, J.; Burke, K.; Ernzerhof, M.; Generalized gradient approximation made simple, *Phys. Rev. Lett.* **1996,** *77*, 3865-3868

[52] Zhou, F.; Cococcioni, M.; Marianetti, C. A.; Morgan, D.; Ceder, G.; First-principles prediction of redox potentials in transition-metal compounds with LDA+U, *Phys. Rev. B: Condens. Matter Mater. Phys.* **2004**, *70*, 235121/1-8

[53] Wang, L.; Maxish, T.; Ceder, G.; Oxidation energies of transition metal oxides within the GGA+U framework, *Phys. Rev. B* **2006**, *73*, 195107

[54] Cabana, J.; Zheng, H.; Shukla, A. K.; Kim, C.; Battaglia, V. S.; Kunduraci, M.; Comparison of the performance of $LiNi_{1/2}Mn_{3/2}O_4$ with different microstructures. *J. Electrochem. Soc.* **2011**, *158*, A997–A1004.

[55] Anderson, P.W.; Ordering and antiferromagnetism in ferrites, *Phys. Rev.* **1956**, *102*, 1008-1013

[56] Lee, E.; Persson, K. A.; Revealing the coupled cation interactions behind the electrochemical profile of $Li_xNi_{0.5}Mn_{1.5}O_4$, *Energy Environ. Sci.*, **2012**, *5*, 6047-6051

[57] Ceder, G.; Aydinol, M.K.; Kohan, A.F.; Application of first principles calculations to the design of rechargeable Li-batteries, *Comp. Mat. Sci.* **1997**, *8*, 161-169

[58] Urban, A.; Seo, D.-H.; Ceder, G.; Computational understanding of Li-ion batteries, *npj Comput. Mat.* **2016**, *2*, 16002/1-13

[59] Idemoto, Y.; Sekine, H.; Ui, K.; Koura, N.; Crystal structural change during charge-discharge process of $LiMn_{1.5}Ni_{0.5}O_4$ as cathode for 5V class lithium secondary battery, *Solid State Ionics* **2005**, *176*, 299-306

[60] Chen, Y.; Sun, Y.; Huang, X.; Origin of the Ni/Mn ordering in high-voltage spinel $Lini_{0.5}Mn_{1.5}O_4$: the role of the oxygen vacancies and cation doping, *Comp. Mat. Sci.* **2016**, *115*, 109-116

[61] Xu, B.; Meng, S.; Factors affecting Li mobility in spinel $LiMn_2O_4$—A first-principles study by GGA and GGA+U methods, *J. Power Sources* **2010**, *195*, 4971-4976

[62] Yi, T.F.; Zhu, Y.-R.; Zhu, R.-S.; Density functional theory study of lithium intercalation for 5V $LiNi_{0.5}Mn_{1.5}O_4$ cathode materials, *Solid State Ionics*, **2008**, *38,* 2132-2136

[63] Boulet-Roblin, L.; Villevieille, C.; Borel, P.; Téssier, C.; Novak, P.; Ben Yahia, M.; Versatile approach combining theoretical and experimental aspects of Raman spectroscopy to investigate battery materials: the case of $LiNi_{0.5}Mn_{1.5}O_4$ spinel, *J. Phys. Chem. C* **2016**, *120*, 16377-16382

[64] McKenna, K.P.; Hofer, F.; Gilks, D.; Lazarov, V.K.; Chen, C.; Wang, Z.; Ikuhara, Y.; Atomic-scale structure and properties of highly stable antiphase boundary defects in Fe_3O_4, *Nature Comm.* **2014**, *5*, 5740-1/8

[65] Cai, L.; Liu, Z.; An, K.; Liang, C.; Unraveling structural evolution of $LiNi_{0.5}Mn_{1.5}O_4$ by *in situ* neutron diffraction, *J. Mater. Chem. A* **2013**, *1*, 6908-6914

[66] Shannon, R.D.; Revised effective ionic radii and systematic studies of interatomic distances in halides and chalcogenides, *Acta Cryst. A* **1976**, *32*, 751-767

[67] McCalla, E.; Rowe, A.W.; Shunmugasundaram, R.; Dahn, J.R.; Structural study of the Li-Mn-Ni oxide pseudoternary system of interest for positive electrodes of Li-ion batteries, *Chem. Mater.* **2013**, *25*, 989-999

[68] Thackeray, M.M.; Mansuetto, M.F.; Dees, D.W.; Vissers, D.R.; The thermal stability of lithium-manganese-oxide spinel phases, *Mat. Res. Bull.* **1996**, *31,* 133-140

[69] Matsuda, Y.; Matsui, M.; Sanda, T.; Takashi, Y.; Imanishi, N.; Low Temperature Synthesis of High Crystalline Spinel Oxides: $LiNi_{1/2}Mn_{3/2}O_4$, *Electrochemistry* **2015**, *83*, 870–873

Table of Content :